

BL1A

Modification of Gallium Oxide Photocatalyst with Mg Ions

K. Shimura¹, T. Yoshida² and H. Yoshida¹

¹ Department of Applied Chemistry, Graduate School of Engineering, Nagoya University, Nagoya 464-8603, Japan

² Department of Materials, Physics and Energy Engineering, Graduate School of Engineering, Nagoya University, Nagoya 464-8603, Japan

The development of a hydrogen production method from renewable resources and natural energy would be important to realize a sustainable society. Photocatalytic steam reforming of methane (PSRM; $\text{CH}_4 + 2\text{H}_2\text{O} \rightarrow 4\text{H}_2 + \text{CO}_2$) is an attractive reaction because it has a potential to produce hydrogen from water and biomethane by using solar energy. We reported that Pt-loaded semiconductor photocatalyst such as Pt/TiO₂ showed activity for this reaction around room temperature [1, 2]. In the present study, we applied the Ga₂O₃ photocatalyst for PSRM and examined the loading effect of Mg ions on the structure and the activity of Ga₂O₃.

Mg²⁺-loaded Ga₂O₃ was prepared from β-Ga₂O₃ and an aqueous solution of Mg(NO₃)₂ by impregnation method, followed by calcination in air at various temperatures for 6 h. Then, Pt (0.01 wt%) co-catalyst was loaded on it by impregnation method followed by calcination in air at 773 K.

Photocatalytic reaction was carried out with a fixed-bed flow type reactor. The quartz cell was filled with the catalyst (0.8 g). The reaction gas (H₂O 1.5%, CH₄ 50%, Ar balance) was introduced at a flow rate of 50 mL min⁻¹, and the light of the entire wavelength region from a 300 W Xe lamp was irradiated. The outlet gas was analyzed by on-line gas chromatography with a thermal conductivity detector.

X-ray absorption spectra were measured in the total electron yield mode at room temperature with a beryl double-crystal monochromator at the BL-1A station of UVSOR-II. The powder sample was put on the first dynode of the electron multiplier with carbon adhesive tape.

Pt/β-Ga₂O₃ promoted PSRM to produce H₂ and CO₂ and the high activity sustained for a long time (Fig. 1a). Further modification of Ga₂O₃ by Mg²⁺ through calcination at 1273 K enhanced the activity (Fig. 1b). However, characterization by XRD, UV-vis and N₂ adsorption exhibited no differences among these samples.

Mg K-edge XANES spectrum of MgO shows some peaks and Ga L₁-edge XANES of Ga₂O₃ was broad spectrum although both absorption edges are known to appear at 1307 eV (Fig. 2 a and f). The spectra of Mg²⁺-loaded Ga₂O₃ samples calcined at various temperatures were much different from each other (Fig. 2 b-d). For the sample calcined at 773 K, the spectrum was similar to that of MgO. When the calcination temperature was higher than 1073 K, the spectra were the same as that of MgGa₂O₄ spinel. It

was suggested that Mg ions would form MgGa₂O₄ spinel-like local structure by substituting for Ga ions at tetrahedral site when the calcination temperature was higher than 1073 K. The Mg ions in the bulk would improve the property of the Ga₂O₃ photocatalyst.

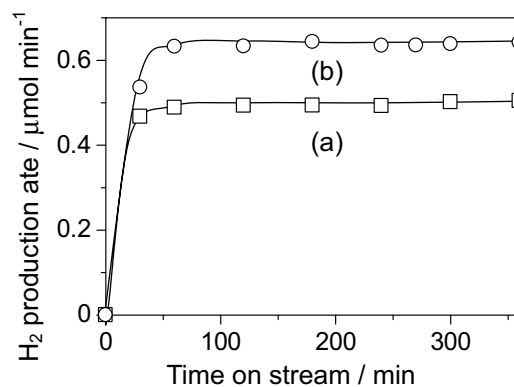


Fig. 1. Time course of the hydrogen production rate over (a) Pt/Ga₂O₃ and (b) Pt/Mg²⁺-loaded Ga₂O₃ prepared at 1273 K.

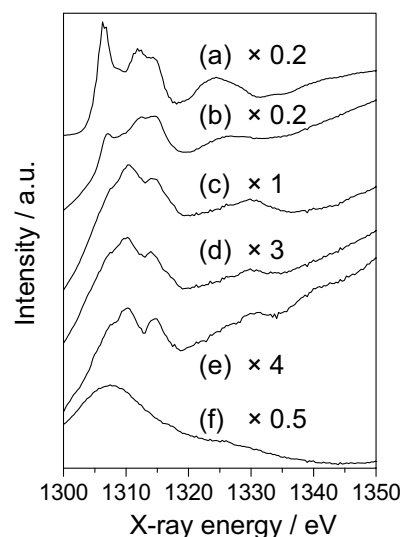


Fig. 2. X-ray absorption spectra of (a) MgO, (b)-(d) Mg²⁺-loaded Ga₂O₃ samples, (e) MgGa₂O₄ and (f) Ga₂O₃. Loading amount was 2 mol%. The calcination temperature was (b) 773 K, (c) 1073 K and (d) 1273 K, respectively.

[1] H. Yoshida *et al.*, Chem. Lett. **36** (2007) 430.

[2] H. Yoshida *et al.*, J. Phys. Chem. C **112** (2008) 5542.

Asymmetric Synthesis and Decomposition of Amino Acids by Using UVSOR-FEL

K. Kobayashi¹, S. Shima¹, T. Suzuki¹, T. Kaneko¹, H. Mita²,
J. Takahashi³, M. Hosaka⁴, M. Adachi⁵ and M. Kato⁵

¹Graduate School and Faculty of Engineering, Yokohama National University,
Yokohama 240-8501, Japan

²Faculty of Engineering, Fukuoka Institute of Technology, Fukuoka 811-0295, Japan

³NTT Microsystem Integration Laboratory, Atsugi 243-0198, Japan

⁴Graduate School of Engineering, Nagoya University, Nagoya 464-8601, Japan

⁵UVSOR Facility, Institute for Molecular Science, Okazaki 444-8585, Japan

Introduction

Amino acids in terrestrial organisms are fundamentally L-enantiomers. A number of hypotheses have been presented on the origin of such biochemical homochirality. One of them is that enantiomeric excesses (e. e.'s) of amino acids were generated by circularly polarized ultraviolet light (CPL-UV) ejected from a neutron star. In order to examine this hypothesis, we irradiated amino acids or metal complexes of amino acids with circularly polarized ultraviolet light (CPL-UV). Isovaline (Fig. 1 a), a non-proteinous amino acid without α -hydrogen atom, was selected as a target amino acid since relatively large e. e. of isovaline was found in Murchison meteorite [1]. A small e. e. formed by CPL-UV might have been enlarged by autocatalytic reactions in primordial ocean. From such a point of view, histidine (Fig. 1 b) was used because it has catalytic activity. Aqueous solution of histidine, isovaline, and metal complexes of them were irradiated with CPL-UV. We also studied possible introduction of chirality to amino acids in thin films by CPL-UV irradiation.

Experimental

The following aqueous solutions in quartz cuvettes were irradiated with CPL-UV light at 217 nm from a free electron laser (FEL) of UVSOR II: DL-Alanine, DL-histidine, Cu-complex of DL-histidine, DL-isovaline and Cu-complex of DL-isovaline. After irradiation, amino acids in the resulting solutions were analyzed by HPLC with chiral columns.

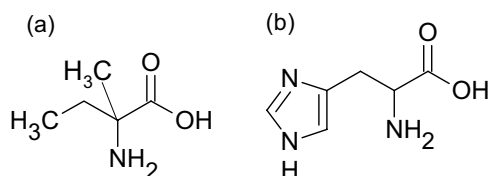


Fig. 1. Isovaline (a) and histidine (b)

Thin films of isovaline and alanine made by vacuum deposition, and they were irradiated with CPL-UV. CD spectra of the resulting thin films were observed.



Fig. 2. CPL-UV irradiation of amino acid solution.

Results and Discussion

Isovaline gave DL-alanine as major amino acid products after irradiation, but only a small part of histidine was decomposed under the present condition. No significant enantiomeric excesses of each amino acid were detected. We irradiated amino acids in neutral solution this time, which might be the reason why no e. e. was found. We are planning to irradiate acidic / basic solution of amino acids and their metal complexes with CPL-UV.

After the irradiation with the CPL on DL-alanine film, peaks appeared in the CD spectra at 180 nm (carboxyl group (π - π^*)) and 215 nm (carboxyl group (n - π^*)) with an opposite sign. Intensity ratio of the two peaks and the intensity and the sign of the CD peaks changed with CPL dose. After the irradiation with the CPL on DL-isovaline film, vague peaks appeared in the CD spectra at 175 nm (carboxyl group (π - π^*)) and 200 nm (carboxyl group (n - π^*)) with an opposite sign. These results suggest that a chiral construction was introduced into the racemic film by the CPL.

[1] J. R. Cronin and S. Pizzarello, *Science* **275** (1997) 951.

Transient Fluorescence Spectroscopy of Dye Sensitized Solar Cells

K. Mitsuke¹, K. Nakajima^{1,2}, H. Katayanagi¹,
 M. Adachi³, T. Tanikawa³, N. Yamamoto⁴, M. Hosaka⁴ and M. Katoh³
¹*Dept. Photo-Molec. Sci., Inst. Molec. Sci., Okazaki 444-8585, Japan*
²*Sci. Res. Center, Hosei Univ., Tokyo 102-8160, Japan*
³*UVSOR Facility, Inst. Molec. Sci., Okazaki 444-8585, Japan*
⁴*Grad. Sch. Engin., Nagoya Univ., Nagoya 464-8603, Japan*

The dye sensitized solar cell (DSSC) has attracted worldwide attention in the last two decades because of its high-solar-energy-to-electricity conversion efficiencies and relatively low cost of its manufacturing. In DSSC solar light is primarily absorbed by a sensitizer dye which is anchored to the surface of a wide band gap semiconductor. The efficiency of sensitization depends critically on the ratio between the rate of electron injection and that of charge recombination. Thus, intensive research has been carried out focusing on the analysis of the dynamics of interfacial electron transfer processes. In this study we assembled a DSSC using a Ru dye and irradiated them with free electron laser (FEL) to observe the kinetics of electron injection using time-resolved fluorescence spectroscopy.

Electron injection is known to occur in a time scale of 10 ps or faster, if TiO₂ film together with Ru dyes is covered in inert solvents. In contrast, the rate of injection is drastically reduced by one or two orders of magnitude in a typical redox active electrolyte. Several authors argued that the additives in the electrolyte used for reducing unwanted electron-hole recombination have an effect of raising the conduction band edge of TiO₂. Eventually the high-efficiency DSSCs often show lifetimes as long as 1 ns with respect to electron injection, that is, injection dynamics which is just fast enough to compete with the fluorescence decay (10 ~ 100 ns) of the excited state of the Ru dyes.

We fabricated the DSSC composed of a nanocrystalline mesoporous TiO₂ film, sensitizer dye ("N719" or "Black dye"), electrolyte (50 mM tri-iodide in acetonitrile, ionic liquid and 4-*tert*-butyl pyridine), and a Pt thin film. All these materials were sandwiched by two electrode plates of FTO glass. The formula of N719 is written as RuL₂(NCS)₂:2TBA (L = 2,2'-bipyridyl-4,4'-dicarboxylic acid; TBA = tetrabutylammonium). Here, dye molecules are firmly grafted onto the surface of the titania through their carboxylate substituents. The assembled DSSC exhibits a maximum energy conversion efficiency of ca. 6.5 %. Fluorescence decay was observed by time-resolved single photon counting using FEL of ~ 580 nm at a repetition rate of 11.3 MHz.

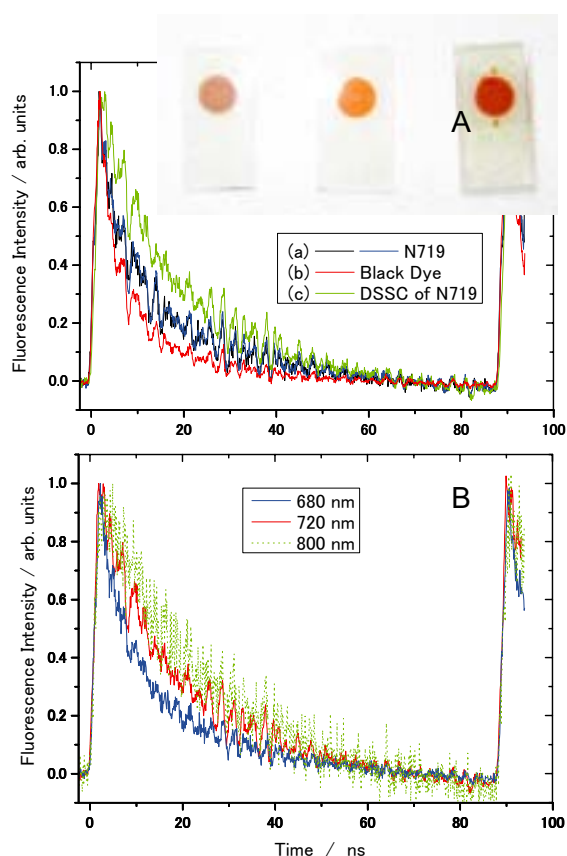


Fig. 1. Fluorescence decay curves of DSSC and photovoltaic electrodes, obtained by FEL photolysis.

Fluorescence decay curves in Fig. 1A were monitored at 720 nm for (a) a photovoltaic electrode of TiO₂ film prepared with N719, (b) that with Black dye, and (c) a complete DSSC fabricated using N719. The apparent fluorescence lifetime of the complete DSSC is longer than those of the two photovoltaic electrodes, probably due to slower electron injection induced by one of the additives in the electrolyte. Figure 1B shows the dependence of the decay curves of the DSSC on the fluorescence wavelength. The rate of electron injection appears to increase with decreasing wavelength. This suggests that the vibrational redistribution of the internal energy in the excited state of the dyes proceeds in competition with the electron injection and fluorescing emission.

This research was partly supported by a grant from Hosei University.

Local Environment Analysis of Al Atoms in Proton-Conducting Amorphous $\text{Al}_{0.1}\text{Si}_{0.9}\text{O}_x$ Thin Films

Y. Aoki and H. Habazaki

Graduate School of Engineering, Hokkaido University, N13W8, Sapporo 060-8628, Japan

Zeolitic compounds are attractive as an unhydrated proton conductor due to the presence of large number of native acid sites. Although gas permeation through the micropore poses difficulty in fuel cell application, they exhibit excellent proton conductivity even in dry atmosphere at elevated temperatures. Previously, we reported that amorphous aluminosilicate thin films exhibit the enhanced proton conductivity in nonhumidified atmosphere in the intermediate temperature range [1]. Amorphous metal oxides have intrinsic advantages for their application to thin film electrolyte, since they tend to be non-granular, dense layer without void formation at grain boundary due to the covalently-bonded M-O-M-O network. Furthermore, we discovered that the films reveal the power-law increment of proton conductivity by reduction of thickness into the sub-100 nm regime [2]. This conductivity scaling behavior was not completely understood, but it is speculated to be involved in the acidic nature of films. Here, we study the local environment of Al atoms in amorphous $\text{Al}_{0.1}\text{Si}_{0.9}\text{O}_x$ thin film thin films by XANES in order to identify the acid site.

The $\text{Al}_{0.1}\text{Si}_{0.9}\text{O}_x$ film was prepared on an ITO substrate (Aldrich) by multiple spin-coating of precursor solutions of tetraethoxysilane (TEOS) (Kanto) and aluminum *sec*-butoxide ($\text{Al}(\text{O}^i\text{Bu})_3$) (Kanto) at the Al/Si atomic ratio of 5/95. The details of the procedure were described elsewhere. [1] The metal concentration (Al+Si) in the precursor mixture sol was adjusted in 30 mM for the film of < 100 nm-thickness and 100 mM for the film of > 100 nm-thickness. A film with thickness of 100 nm was prepared from both of these sols. The precursor sols were spin-coated onto the ITO substrate at 3000 rpm for 40 sec by a Mikasa 1H-D7 spin coater. The deposited gel layer was hydrolyzed by blowing hot air for 30 sec (Iuchi hot gun), and the substrate was cooled to room temperature by blowing cold air for 20 sec. These cycles of spin-coating, hydrolysis and cooling were repeated 10-20 times and the gel film thus obtained was calcined at 400°C for 15 min. The combination of deposition and calcination was repeated more than 3 times, and the final calcination was performed at 450°C for 1 h.

Al K-edge XANES spectroscopy was carried out with $\text{Al}_{0.1}\text{Si}_{0.9}\text{O}_x$ films of 50 nm, 120 nm and 300 nm-thickness (Fig. 1). It is reported that Al K-edge spectra is very sensitive to the coordination number and geometry of AlO_x moieties in oxides. [3] Here, the Y-zeolite (Wako) was used as a reference material of tetrahedral AlO_4 configuration and $\alpha\text{-Al}_2\text{O}_3$ (Wako) as

that of octahedral AlO_6 configuration, respectively. Y-zeolite shows a sharp peaks at 1566 eV and a broad peak at 1571 eV in agreement with the spectral features of tetrahedral AlO_4 compounds. $\alpha\text{-Al}_2\text{O}_3$ shows two sharp peaks at 1568 and 1572 eV, which are identical to the features of the compound given by the previous reports. The $\text{Al}_{0.1}\text{Si}_{0.9}\text{O}_x$ films possess the same features of XANES in every thickness. They show a sharp peak at 1566 eV and a broad peak at 1571 eV, which are identical to that of Y-zeolite. Therefore, it is clear that Al atom in these films preferably takes the tetrahedral AlO_4 configuration. These results suggest that $\text{Al}_{0.1}\text{Si}_{0.9}\text{O}_x$ films have the zeolite-like aluminosilica network, where the SiO_4 tetrahedron and AlO_4 tetrahedron are 3-dimensionally linked by corner-sharing. Thus, our films can retain amounts of Brønsted acid site by the protonation onto the negative charge of -Si-O-Al- hetero bond as is the case with zeolite.

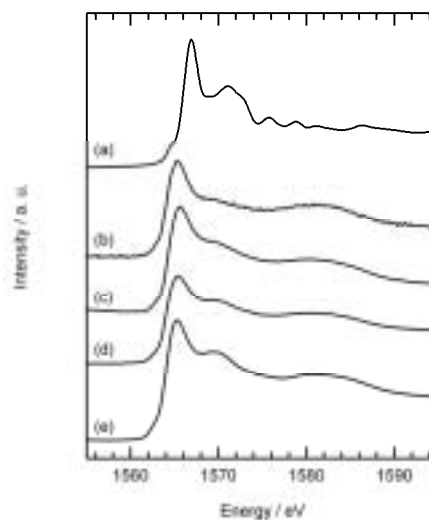


Fig. 1. Al K-edge XANES spectra of amorphous $\text{Al}_{0.1}\text{Si}_{0.9}\text{O}_x$ films and reference materials. (a) $\alpha\text{-Al}_2\text{O}_3$ powder, (b) 300 nm-thick film, (c) 120 nm-thick film, (d) 50 nm-thick film and (e) Y-zeolite powder.

- [1] Y. Aoki *et al.*, Adv. Mater. **20** (2008) 4387.
 [2] Y. Aoki *et al.*, Electrochem. Solid state Lett. **11** (2008) 13.
 [3] Y. Kato *et al.*, PCCP **3** (2001) 1925.

Mo L_{III}-Edge XANES Study on Redox Behavior of Supported Mo Species on H-MFI for Methane Dehydroaromatization Catalysts

H. Aritani¹, K. Nagashima¹, M. Morioka¹, H. Shibasaki¹ and A. Nakahira²

¹Faculty of Engineering, Saitama Institute of Technology, Fukaya 369-0293, Japan

²Graduate School of Engineering, Osaka Prefecture University, Sakai 599-8531, Japan

MoO₃-modified H-MFI catalyst is typical for exhibiting quite high activity and selectivity for CH₄ dehydroaromatization in absence of oxygen. On the reaction, reduction of Mo species is brought about in contact with methane in initial step. The Mo ions react methane to form carbide and/or oxycarbide species in the next step. The carbide species is active for methane dehydroaromatization, however, deactivation is brought about by carbon deposition on the catalyst surface at the same time. Therefore, red-ox performance of active Mo ions (such as Mo²⁺ and others) is one of a key role for catalytic dehydroaromatization activity. In our previous study, pretreatment with CO and H₂ co-feed with CH₄ reactant give a significant effect for high activity. However, excess hydrogen may affect a reduction of Mo species during the reaction. Thus, the effect of hydrogen with methane is also very important to give an effect on Mo state on H-MFI. This study addresses the effects of CO pretreatment and H₂ co-feed with CH₄ reactant for Mo sites on H-MFI. Characterization by Mo L_{III}-edge XANES can be applied to evaluate the red-ox performances of Mo sites in detail.

Catalysts were prepared by impregnation of H-MFI (Si/Al₂=72) synthesized hydrothermally with MoO₂(acac)₂-CHCl₃ solution, and followed by drying overnight and calcination at 773 K. MoO₃-loading amount is 5.0 wt% in all the catalysts. Mo L_{III}-edge XANES spectra were collected in BL1A of UVSOR-IMS in a total-electron yield mode using InSb double crystal monochromator. Photon energy was calibrated by using Mo metal-foil at Mo L_{III}-edge, and normalized XANES spectra and their second derivatives were obtained. Catalytic activity was evaluated in a fixed bed flow reactor. Each catalyst (0.25 g) was placed in a quartz-tube reactor, and pretreated in He-CO(0-2%) flow (30 mL min⁻¹) at 973 K for 1 h. Then CH₄(20%)-H₂(0-3%)-He reactant gas was fed at 973 K (30 mL min⁻¹; SV = 7.2 L g⁻¹ h⁻¹). Products were analyzed by online GC.

After pretreatment with CO (shown in Fig. 1(A)) at 973 K, small amount of reduced Mo is formed. After the reaction with CH₄ or CH₄-H₂ (Fig. 1(B)(C)), reduced Mo (Mo²⁺ in major) species because of the large intensity of minimum peaks (at 2522.5 eV) of 2nd derivatives of L_{III}-XANES spectra [1]. The reduced Mo species after the reaction is not similar to bare Mo₂C, suggesting the formation of carbonized MoC_x species [2]. In these cases, the catalysts are almost deactivated by contamination of hydrocarbon

and/or carbon deposition. After the following treatment with H₂(2%)-He or He, the amount of deposited species decreased by species, whose results are evaluated by thermogravimetry. In addition, catalytic activity is restored by their treatments. On these cases (Fig. 1(D)(E)), the ratio of reduced (carbonized) Mo species becomes small. These results suggest that carbonized Mo species are formed on H-MFI after the CH₄ dehydroaromatization, and excess carbon and/or hydrocarbon species are deposited on Mo sites as MoC_x species. By not only H₂ but also He treatments, excess carbonaceous species can be desorbed and restore the dehydroaromatization activity. It is concluded that deactivation can exhibit the gas treatment with no red-ox atmosphere because of enhancement of desorption of carbonaceous species.

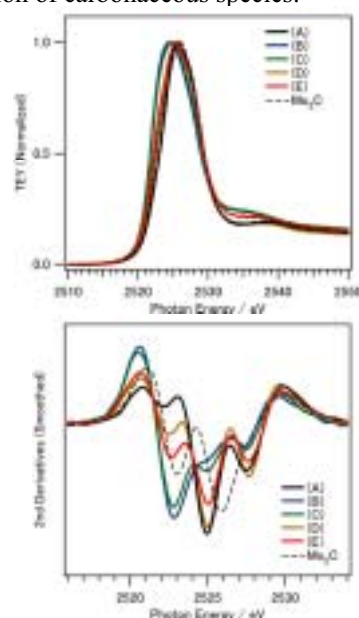


Fig. 1. Mo L_{III}-edge XANES spectra (top) and their second derivatives (bottom) of 5.0 wt% MoO₃-modified H-MFI (Si/Al₂=72) catalysts. (A) After CO(2%)-He pretreatment; (B) After reaction with CH₄(20%)-He on sample (A); (C) After H₂(2%)-He treatment on sample (B); (D) After reaction with CH₄(20%)-H₂(2%)-He on sample (C); (E) Reacted with CH₄(20%)-He on sample (A), and then He treated and followed by reaction with CH₄(20%)-H₂(2%)-He.

[1] H. Aritani *et al.*, UVSOR Activity Report **35** (2008) 106.

[2] H. Aritani *et al.*, J. Environm. Sci., in press.

Characterization of Various Phosphate Compounds by an XAFS Method

T. Kurisaki¹, D. Tanaka¹, Y. Sakogawa¹ and H. Wakita²

¹ *Department of Chemistry, Faculty of Science, Fukuoka University, Jonan-ku, Fukuoka 814-0180, Japan*

² *Advanced Materials Institute, Fukuoka University, Jonan-ku, Fukuoka 814-0180, Japan*

A phosphate compound is a very important compound constituting DNA and ATP. In addition, these compounds have widely used such as production of the manure, a catalyst of the ethylene production, cement for dentistry, a metal surface treatment agent, the coagulant of the rubber milky liquid, and medicine. For various light element compounds, we have studied the electronic structure by X-ray absorption spectroscopy [1,2,3]. These results suggested that there is a correlation between XANES spectra and the local structures.

In this work, we applied the X-ray absorption near edge structure (XANES) spectroscopy to phosphate compounds. The results of the measurement indicate unoccupied and occupied electronic structure of phosphate compounds. The X-ray absorption spectra were measured at BL1A of the UVSOR in the Institute of Molecular Science, Okazaki [4]. The ring energy of the UVSOR storage ring was 750 MeV and the stored current was 110-230 mA. P K-edge absorption spectra were recorded in the regions of 2125-2270 eV by use of two InSb crystals. The absorption was monitored by the total electron yield using a photomultiplier. The samples were spread into the carbon tape on the first photodynode made of CuBe of the photomultiplier.

Figure 1 shows the observed P K-edge XANES spectra for the phosphate compounds. The P-K XANES spectra of hydroxyapatite, octacalcium phosphate, and standard phosphate compounds show different peak profiles. These phosphate compounds have different electronic state. We are going to try to calculate the spectra by DV-X α molecular orbital calculations.

[1] H. Ichihashi, T. Kurisaki, T. Yamaguchi, T. Yokoyama and H. Wakita, *Jpn. J. Appl. Phys. Part 1* **38(suppl.)** (1999) 101.

[2] S. Matsuo, K. Shirouzu, Y. Tateishi and H. Wakita, *Adv. Quan. Chem.* **42** (2002) 407.

[3] T. Kurisaki, Y. Nakazono, S. Matsuo, R.C.C. Perera, J. H. Underwood and H. Wakita, *Adv. Quantum Chem.* **54** (2008) 315.

[4] S. Murata, T. Matsukawa, S. Naoè, T. Horigome, O. Matsudo and M. Watatabe, *Rev. Sci. Instrum.* **63** (1992) 1309.

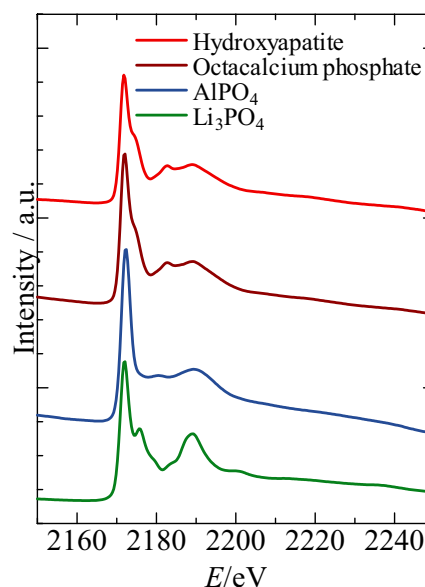


Fig. 1. Observed Al K-edge XANES spectra of phosphate compounds.

Defect Formation Mechanism in $\text{Ce}_{1-x}\text{Y}_x\text{O}_{2-x/2}$

Y. Nakade and T. Yamamoto

Faculty of Science and Engineering, Waseda University, Shinjuku 169-8555, Japan

$\text{Ce}_{1-x}\text{Y}_x\text{O}_{2-x/2}$ is known as a solid oxide electrolyte of fuel cell, which shows high oxygen ion conductivity. In order to know the reasons for this high conductivity, it is essential to know the defect formation mechanism in $\text{Ce}_{1-x}\text{Y}_x\text{O}_{2-x/2}$. In the present study, the local environment of Y^{3+} ions in CeO_2 was examined by the Helmholtz free energies and XANES.

$\text{Ce}_{1-x}\text{Y}_x\text{O}_{2-x/2}$ was synthesized by CeO_2 and Y_2O_3 powders with the solid state reaction method. XANES measurements were carried out at BL-1A of UVSOR with double-crystal monochromator using InSb (111) ($2d = 7.481\text{\AA}$) in the total electron yield method.

Four types of defect models were built by changing the positions of two Y ions and O vacancy according to the reaction $[2\text{Ce}^{4+} \leftrightarrow 2\text{Y}^{3+} + \text{V}_\text{O}]$, which are shown in Fig. 1. In Y-O-Y and Y-Y models, two nearest neighboring Ce^{4+} are replaced by two Y^{3+} ions and an oxygen ion is removed between these two substituted Y^{3+} ions (Y-O-Y model) and at distant position from these Y^{3+} ions (Y-Y model). In Distant and Y-O models two distant Ce^{4+} ions are replaced by Y^{3+} ions and an oxygen ion is removed at the first nearest neighboring site from one of the substituted Y^{3+} ions (Y-O model), and at a distant site from both of the substituted Y^{3+} ions (Distant model).

We calculated Helmholtz free energies by the first principles PAW method in order to compare the relative defect formation energy among these models. Helmholtz free energy, $F=U-TS$, is obtained, where U is treated as a total electronic energy at 0K, S was calculated by $S=k_B \ln W$, in which W is atomic configurations in the system, and k_B and T are Boltzmann constant and temperature. Resultant F are -833.54, -833.50, -833.40 and -833.24 eV per supercell for Distant, Y-O, Y-Y, and Y-O-Y models, respectively, at 1773K, which is a present synthesized temperature. This result suggests two Y^{3+} ions and an oxygen vacancy are located apart as in Distant model.

We also performed XANES analysis. The first principles calculations for these four models within the density functional theory (DFT) were performed for the theoretical estimation of the XANES spectra with the all-electron linearized augmented plane wave package, WIEN2k [1]. Figure 2 shows the comparison between observed and four calculated XANES spectra of Y L_{III}-edge of $\text{Ce}_{1-x}\text{Y}_x\text{O}_{2-x/2}$. As shown in this figure Distant and Y-Y models, where the coordination number of two Y^{3+} ions is 6, show better comparisons than the others [2]. This result supports the above result by calculated Helmholtz free energy.

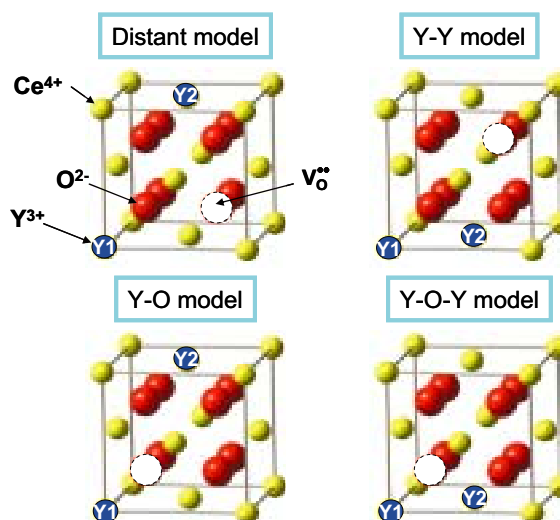


Fig. 1. Calculated models for $\text{Ce}_{1-x}\text{Y}_x\text{O}_{2-x/2}$.

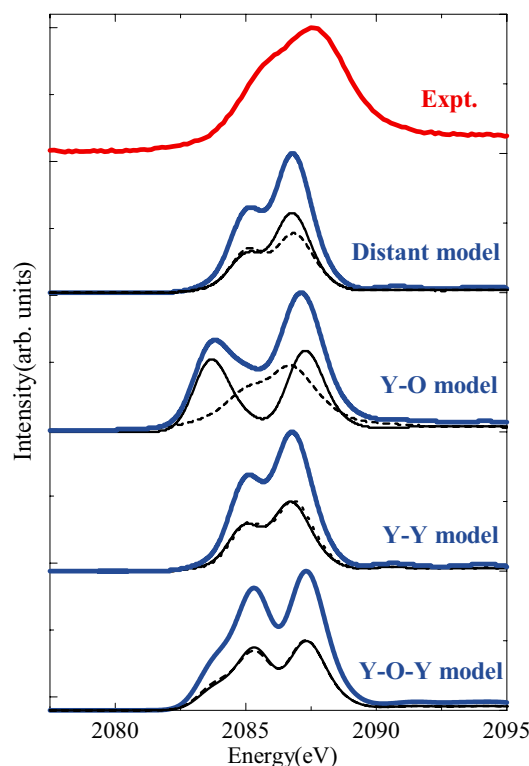


Fig. 2. Comparison between observed and calculated XANES spectra of Y L_{III}-edge of $\text{Ce}_{1-x}\text{Y}_x\text{O}_{2-x/2}$.

[1] P. Blaha *et al.*, <http://www.wien2k.at>

[2] T. Yamamoto *et al.*, J. Phys.:Condens. Matter, in press.

Mg Local Structure in Ca,Mg Doped ZrO₂ for Artificial Joints with Good Biocompatibility

A. Nakahira, T. Monden T. Kubo and T. Onoki

Faculty of Engineering, Osaka Prefecture University, Gakuencho, Sakai 599-8531, Japan

Introduction

Because ZrO₂ is one of high performance bioceramics with good properties, it is used as a biomaterial like knee and hip joints [1]. Many papers have investigated for Y₂O₃ or CeO₂ doped ZrO₂ due to their excellent mechanical properties. Y₂O₃ doped ZrO₂ and CeO₂ doped ZrO₂ have the good mechanical properties, such as high fracture toughness, high fracture strength, good wear resistance, high hardness, and good fatigue resistance etc.

Recently, the addition of Y and Ce into ZrO₂ raises question about the point of biological safety, although Y₂O₃ doped ZrO₂ and CeO₂ doped ZrO₂ have excellent mechanical properties. Therefore, the development of another element doped ZrO₂ are desired. For example, in this study, CaO and MgO which are considered to be more biocompatible material, compared to Y₂O₃ and CeO₂, were selected as stabilizers for ZrO₂ based biomaterial. Moreover, in order to improve the mechanical properties of ZrO₂, we attempted to fabricate co-doped CaO and MgO to ZrO₂ by the spark plasma sintering (SPS) method in this study. At UVSOR station, we measured XANES of CaO,MgO-ZrO₂ prepared by the spark plasma sintering (SPS) method. The main purpose is to investigate the relationship between mechanical properties, microstructures and Mg local structure.

Experiments

Commercial CaO, MgO, and ZrO₂ powder were prepared as starting materials. Mixture of powder was mixed with wet ball-milling method. The mixed powders for CaO,MgO-ZrO₂ powders were sintered at 1300°C by the spark plasma sintering (SPS) method.

Obtained samples were identified by XRD and SEM observation. Mg K-edge XANES spectra were obtained in a total electron yield mode at room temperature using KTP double-crystal monochromator at BL01A station of the UVSOR. The spectra were collected in the photon energy range from 1300 to 1330 eV at intervals of 0.05 eV with a dwell time of 1 s.

Results

10Ca-10Mg-ZrO₂ had high hardness but the low

fracture toughness with coarse microstructures. Figure 1 shows the results of Mg K-edge XANES of CaO,MgO-ZrO₂ prepared by the spark plasma sintering (SPS) method: a) 3Ca and 3Mg, b) 5Ca and 5Mg, c) 10Ca and 10Mg doped, respectively. As the spectrum of the samples was obviously different between a), b) and c), there is some difference of chemical bonding of Mg between three CaO,MgO-ZrO₂ samples. Therefore, it is estimated that the microstructures are dependent on amount of dopant (Mg and Ca). These results of XANES spectra suggested that the Mg local structures influence mechanical properties and microstructures for CaO,MgO-ZrO₂.

[1] J. M. Brown, B. Cales, J. Chevalier and G. Fantozzi, *Journal of Biomedical Materials research* **34** (1997) 149.

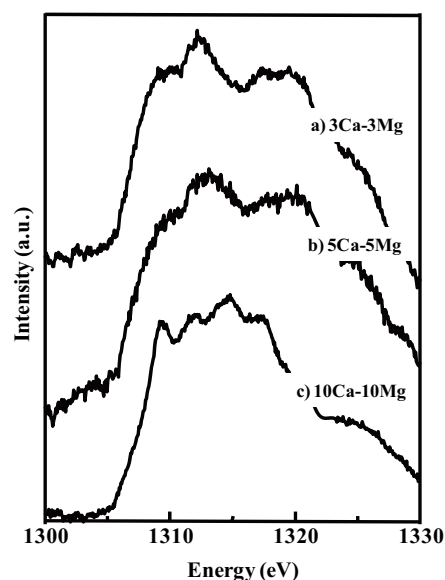


Fig. 1. Mg K-edge XANES spectra of ZrO₂ prepared by SPS method.

Cation Disorder in Quenched MgFe_2O_4 Spinel

T. Nakashima and T. Yamamoto

Faculty of Science and Engineering, Waseda University, Shinjuku 169-8555, Japan

Magnetic properties of spinel-type oxides containing transition metal ions depend on the local environment of magnetic ions, especially the cation distribution in octahedral and tetrahedral sites [1, 2]. For the detailed understanding of the magnetic properties of these materials, it is crucial to know the cation distribution on an atomic scale. X-ray absorption near-edge structure (XANES) spectra have been widely used for the characterization of the electronic structures since it is sensitive to change in their local environment such as coordination number. In this study, the quenched MgFe_2O_4 spinels were investigated by utilizing Vibrating Sample Magnetometer (VSM) and XANES.

MgFe_2O_4 samples are synthesized by the conventional solid-state reaction method. The samples were annealed for 2 hours at intervals of 100 K from 973 K to 1273 K and then dropped in H_2O . Mg-K XANES spectra were observed at BL1A in UVSOR by the total electron yield (TEY) method. The incident beam was monochromatized with a beryl (10 $\bar{1}$ 0) ($2d = 15.965 \text{ \AA}$) double crystal monochromator.

Prior to the VSM and XANES analysis, all the samples were characterized by the X-ray diffraction (XRD), in which no extra peaks can be found except for those of the spinel structured MgFe_2O_4 .

The magnetic properties of the prepared samples were examined by VSM. The saturated magnetization increases incrementally with annealing temperature as shown in Fig. 1. It is considered that this variation of magnetic properties with annealing temperature reflects the change of the degree of cation disorder.

Observed Mg-K XANES spectra of the quenched MgFe_2O_4 spinels are shown in Fig. 2. The relative intensity of peak C decreases incrementally with annealing temperature up to 1273 K. This phenomenon suggests that the change in XANES spectra reflect the degree of cation disorder. Observed Mg-K XANES is the sum of those from Mg^{2+} ions at octahedral and tetrahedral sites. This change in the intensity of peak C should originate from the change in the ratio of the Mg^{2+} sites between octahedral and tetrahedral sites. From these experimental results we could conclude that Mg-K edge XANES spectra for the quenched MgFe_2O_4 spinels reflect magnetic properties. Thus, this combination of the VSM and XANES analysis with the assistance of XRD must be powerful tool to investigate the cation disordering in the spinel structured materials.

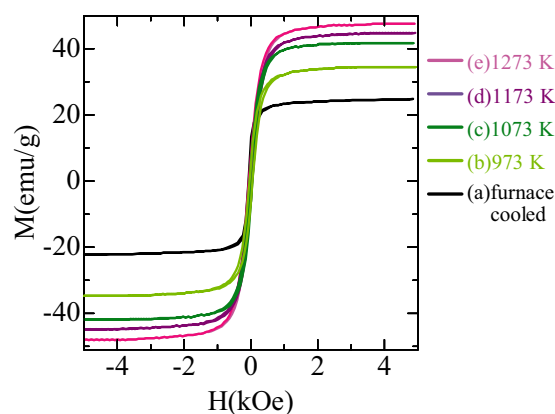


Fig. 1. Observed magnetization versus magnetic field curve of (a) furnace cooled MgFe_2O_4 and the samples quenched at (b) 973 K, (c) 1073 K, (d) 1173 K and (e) 1273 K.

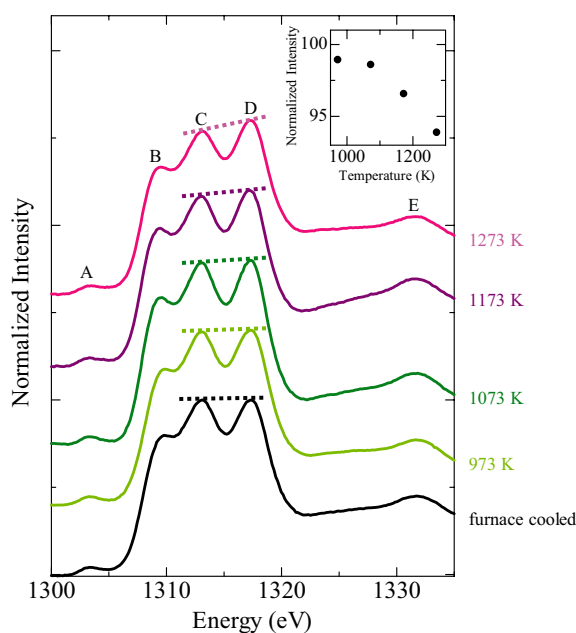


Fig. 2. Observed XANES spectra at Mg K-edge for MgFe_2O_4 spinels. Inset shows the relative intensity of peak C to that of furnace cooled one as a function of quenched temperature.

- [1] S. Nakashima *et al.*, *J. Magn. Magn. Mater.* **310** (2007) 2543.
- [2] H. St. C. O'Neil, *Eur. J. Mineral.* **4** (1992) 571.

XAFS Study on the Surface Structures of the Positive Electrodes for High Power-Type Lithium-Ion Battery Cells

M. Shikano¹, H. Nitani¹ and Y. Saito²

¹Research Institute for Ubiquitous Energy Devices, AIST, Ikeda, Osaka 563-8577, Japan

²Energy Technology Research Institute, AIST, Tsukuba, Ibaraki 305-8568, Japan

Introduction

Lithium-ion battery is a key component of hybrid electric vehicle (HEV), plug-in HEV and electric vehicle (EV). For these applications, high specific power, long calendar life and safety are very important requirements. In our previous work, degradation mechanism of lithium-ion battery has been studied by various analyzing techniques and we concluded that the major factor of power fade was degradation of positive electrode surface [1-4]. However, the mechanism of degradation of the positive electrodes is still poorly understood. Detailed analysis on the structural changes of electrode material is essential in order to determine the origin of the degradation of battery performance.

In this study, we performed X-ray absorption fine structure (XAFS) analysis of $\text{LiNi}_{0.80}\text{Co}_{0.15}\text{Al}_{0.05}\text{O}_2$ positive electrodes in order to obtain information on their surfaces. The relationship between power fade and the surface structure of the positive electrode was studied.

Experimental

18650-type cylindrical lithium-ion cells with a capacity of 370 mAh were manufactured. Mixture of $\text{LiCo}_{0.15}\text{Ni}_{0.80}\text{Al}_{0.05}\text{O}_2$, acetylene black and poly vinylidene fluoride (PVDF) was used as positive electrode. The negative electrode was composed of hard carbon and PVDF. A 1 mol dm^{-3} of LiPF_6 in ethylene carbonate and dimethyl carbonate (DMC) in the 1:2 volume ratio was used as electrolyte. The state of charge (SOC) of assembled cell was adjusted to 0% or 100%. Then the cells were disassembled in order to obtain electrode materials. The obtained positive electrodes were washed by DMC and then dried under vacuum. We also prepared 'fresh' electrode by disassembling the cell before charging.

XAFS spectra of these positive electrodes were measured at UVSOR BL1A for P *K*-edge, Al *K*-edge, Ni *L*-edge and Co *L*-edge, and BL8B1 for O *K*-edge, F *K*-edge and Li *K*-edge. All measurements were performed with Total Electron Yield (TEY) technique at room temperature. Obtained XAFS spectra data were processed with Athena 0.8.057 software.

Results

Obtained P *K*-edge XANES spectra of the positive electrodes are shown in Fig. 1 with that of reference materials, LiPF_6 , Li_3PO_4 , LiFePO_4 and $\text{NH}_4\text{H}_2\text{PO}_4$. The spectrum of fresh electrode clearly indicated double peak feature at 2172.5 and 2177.5 eV. Though the SOC of electrode was changed, this double peak

feature maintained and intensity of 1st and 2nd peak were almost same as fresh electrode. The peak position of 1st peak was close to $\text{NH}_4\text{H}_2\text{PO}_4$. And none of reference materials showed any peaks at 2nd peak position. Essentially, positive electrode material does not contain any P species. So, existence of P in positive electrode means adsorption of P species from electrolyte. However, electrolyte involves only LiPF_6 which was not observed in XANES measurements. From these results, we concluded that the adsorbed LiPF_6 reacted at the surface of positive electrode and changed into other chemical species. The more detailed structural analysis will be studied.

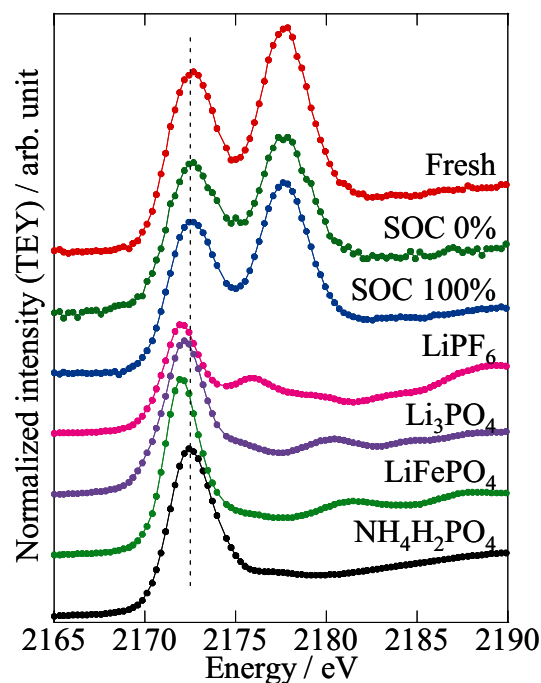


Fig. 1. P *K*-edge XANES spectra of positive electrodes and some reference materials. All spectra were normalized by Athena software.

- [1] H. Kobayashi, M. Shikano, S. Koike, H. Sakaebe and K. Tatsumi, *J. Power Sources* **174** (2007) 380.
- [2] M. Shikano, H. Kobayashi, S. Koike, H. Sakaebe, E. Ikenaga, K. Kobayashi and K. Tatsumi, *J. Power Sources* **174** (2007) 795.
- [3] M. Rahman and Y. Saito, *J. Power Sources* **174** (2007) 889.
- [4] Y. Saito and M. Rahman, *J. Power Sources* **174** (2007) 877.

Luminescent Properties of BaCl₂ under VUV Excitation

M. Koshimizu, K. Onodera and K. Asai

Department of Applied Chemistry, Graduate School of Engineering, Tohoku University, Sendai, 980-8579, Japan

In recent years, the demand for fast scintillating materials has increased for applying in radiation detectors with an excellent timing property and the ability to operate at a high counting rate. BaCl₂ is one of the promising candidates for such fast scintillating materials. In 1990, a fast scintillation component with a relatively high efficiency was reported for BaCl₂ powder under X-ray irradiation [1]. Our recent research on the scintillation properties of a BaCl₂ single crystal revealed that this crystal includes a fast scintillation component of approximately 1.5 ns, and the timing property of BaCl₂ is comparable to that of a conventional fast scintillating material such as BaF₂ [2]. According to our previous study, the scintillation of BaCl₂ ranged over wavelengths region of 250–500 nm, and its spectra exhibited two distinct peaks at approximately 300 and 400 nm. In addition, it was revealed that the scintillation time profile comprised two lifetime components in the nanosecond regime, i.e., a 1.5-ns component and another of the order of tens of nanoseconds. However, the origin of the scintillation in BaCl₂ has not been revealed yet, and understanding the origin of scintillation is necessary in order to improve the scintillation properties of BaCl₂. In particular, it may be anticipated that the 1.5-ns component is ascribed to Auger-free luminescence because of its short lifetime and the scintillation wavelength in the UV region [2]. In this study, we present the luminescent properties of BaCl₂ under synchrotron VUV excitation, and discuss the origin of the emission.

A single crystal of BaCl₂ was grown by the Bridgman method. The emission and excitation spectra of BaCl₂ were measured at room temperature under the irradiation of synchrotron radiation having energies of 4–32 eV at the UVSOR facility (BL-1B).

Figure 1 shows the emission spectra of BaCl₂ under VUV excitation. Under 162-nm photon excitation, an emission band at 410 nm and a shoulder at 350 nm were observed. In contrast, an emission near 310 nm was observed under 176-nm photon excitation.

Figure 2 shows the excitation spectra for the emission bands at 410 nm and 310 nm. The 410-nm emission was observed over the broad excitation wavelength region including the sub-bandgap energy, suggesting that this band is caused by defects or impurities. The 160-nm sharp band of the excitation spectrum corresponds to the interband excitation. The excitation peak at 70 nm corresponds to twice the band-gap energy, suggesting that two electron-hole (e-h) pairs were created by one photon due to the impact ionization of the initially-excited

e-h pair. The 310-nm emission was observed only for the near band-edge excitation, possibly corresponding to exciton absorption. This emission is considered to be an intrinsic one because this band was not observed under sub-bandgap excitation. Considering its large Stokes shift, this band is likely caused by impurities, defects, or self-trapped excitons. Thus, two emission bands are not ascribed to the Auger-free luminescence.

[1] S.E. Derenzo *et al.*, Conference Record of the 1991 IEEE, **1** (1991) 143.

[2] M. Koshimizu *et al.*, submitted to J. Appl. Phys.

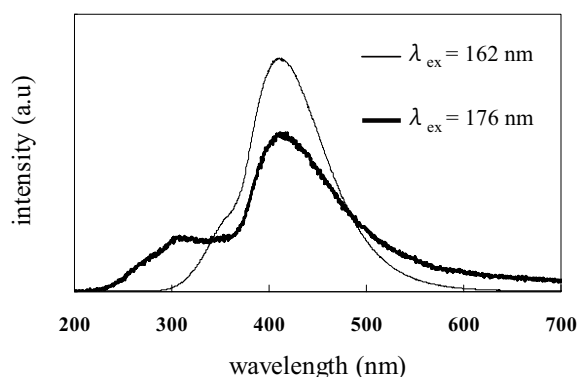


Fig. 1. Emission spectra of BaCl₂ under VUV excitation.

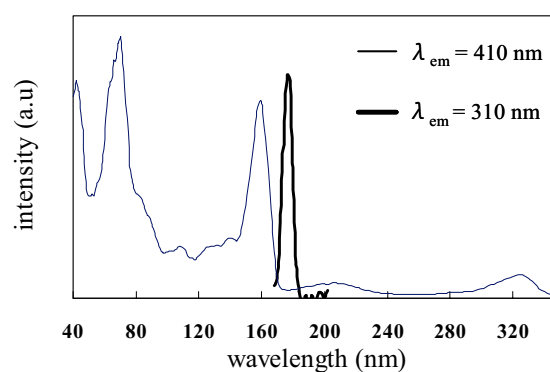


Fig. 2. Excitation spectra of BaCl₂ under VUV excitation.

Luminescence Properties of $\text{GdBO}_3:\text{Pr}^{3+}, \text{Eu}^{3+}$

N. Ohno and K. Kohmoto

*Division of Electronics and Applied Physics, Graduate School of Engineering,
Osaka Electro-Communication University, Neyagawa, Osaka 572-8530, Japan*

Recently, the phosphors to convert vacuum ultraviolet (VUV) light into visible light, which are used in mercury-free fluorescent lamps and plasma display panels, have been researched extensively. The materials with higher quantum efficiency for VUV light emitted from Xe dimers (173 nm) or monomers (147 nm) are quite needed.

Most borate hosts are transparent up to 140-180 nm, so that the VUV light can directly excite impurity activator in these hosts [1,2]. The strong absorption due to the impurity ions would give efficient conversion of the VUV light.

In the present study, luminescence properties of trivalent rare earth metal ion center in gadolinium borate have been studied in the UV and VUV region. The $\text{GdBO}_3:\text{Pr}^{3+}, \text{Eu}^{3+}$ ($\text{GdBO}_3:\text{Eu}^{3+}$) phosphors were prepared by amounts of the appropriate starting compound powders of GdBO_3 adding and mixing Pr_2O_3 and Eu_2O_3 (1 mol %), and then firing in an alumina crucible at 1100°C in the air atmosphere [3]. The impurity Pr^{3+} and Eu^{3+} ions would be substituted for Gd^{3+} ions in the host lattices.

Figure 1 shows the luminescence (red curve) and the photo-excitation (blue curve) spectra of $\text{GdBO}_3:\text{Pr}^{3+}, \text{Eu}^{3+}$ measured at room temperature. Luminescence peaks located at around 600 nm are observed for the excitation of UV and VUV light. These luminescence peaks are attributed to the $f-f$ transition from 5D_0 state to 7F_j states in Eu^{3+} ion. It should be noted that no luminescence peaks due to Pr^{3+} ions were observed in this phosphor. The luminescence spectrum is almost the same as that of $\text{GdBO}_3:\text{Eu}^{3+}$ phosphor [4].

The luminescence due to Eu^{3+} ions is excited with lights of 275 nm, ~ 230 nm and 175 nm (blue curve in Fig.1). These excitation peaks are located at longer wavelength than the absorption edge of the host GdBO_3 (around 150 nm). The excitation band at around 225 nm is attributed to the $\text{Eu}^{3+}-\text{O}^{2-}$ charge transfer transition in Eu^{3+} ion [4]. The excitation line at 275 nm was also observed in $\text{GdBO}_3:\text{Eu}^{3+}$, attributed to the transition from 8S to 6I state in Gd^{3+} ion. This indicates that the energy transfer from Gd^{3+} to Eu^{3+} ions occurs in $\text{GdBO}_3:\text{Eu}^{3+}$ and $\text{GdBO}_3:\text{Pr}^{3+}, \text{Eu}^{3+}$.

The excitation band at 175 nm would be ascribed to the $f-d$ transition in Pr^{3+} ions since the structure is hardly observed in the excitation spectrum for the phosphor without Pr^{3+} ions, *i.e.* $\text{GdBO}_3:\text{Eu}^{3+}$. These results clearly show that the VUV light absorption in Pr^{3+} ions gives the red luminescence due to Eu^{3+} ions. It is concluded that the energy transfer from Pr^{3+} ions

to Eu^{3+} ions through Gd^{3+} sublattices effectively occurs in $\text{GdBO}_3:\text{Pr}^{3+}, \text{Eu}^{3+}$ as in the case of $\text{NaGdF}_4:\text{Pr}^{3+}, \text{Eu}^{3+}$ phosphor [5].

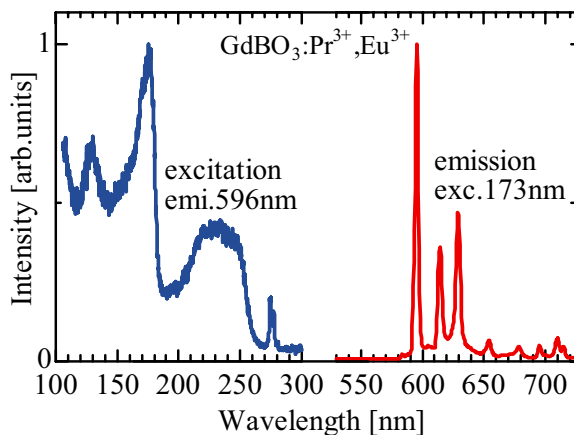


Fig. 1. Luminescence (red curve) and photo-excitation (blue curve) spectra of $\text{GdBO}_3:\text{Pr}^{3+}, \text{Eu}^{3+}$ at room temperature.

- [1] H. Lin, H. Liang, B. Han, J. Zhong, Q. Su, P. Dorenbos, M.D. Birowosuto, G. Zhang, Y. Fu and W. Wu, *Phys. Rev. B* **76** (2007) 035117.
- [2] N. Ohno and K. Kohmoto, *UVSOR Activity Report* **35** (2008) 82.
- [3] X.C. Jiang, C.H. Yan, L.D. Sun, Z.G. Wei, C.S. Liao, *J. Solid State Chem.* **175** (2003) 245.
- [4] T. Kim and S. Kang, *Mater. Res. Bull.* **40** (2005) 1945.
- [5] T. Hirai and N. Ohno, *UVSOR Activity Report* **28** (2001) 116.

Optical Spectroscopy of YAG Ceramics Doped with Rare-Earth Ions

M. Yamaga, Y. Oda and N. Kashiwagura

Department of Mathematical and Design Engineering, Gifu University, Gifu 501-1193, Japan

Recently, ceramic lasers have been attractive since 1995 because ceramics can be produced in large volumes, made into composite media with complicated structures, and heavily and homogeneously doped with laser-active ions. Ceramic lasers with high power density and high resistance to laser damage are very useful for energy conversion system from inexhaustible solar energy to other optical energy. Absorption spectra of Cr^{3+} ions in ionic crystals, for example, $\text{Y}_3\text{Al}_5\text{O}_{12}$ (YAG) crystals cover the visible range (400-700 nm). YAG ceramics codoped with Nd^{3+} and Cr^{3+} ions are renewed as a laser medium with excitation of solar energy because of highly efficient energy transfer from Cr^{3+} to Nd^{3+} ions.

YAG ceramics codoped with 1at. % Nd^{3+} and 0.1 at. % Cr^{3+} were sintered by Konoshima Chemical Company. Optical absorption, fluorescence and excitation spectra were measured in the temperature range of 10-300 K.

Figure 1 shows the temperature dependence of optical absorption spectra in Nd:YAG and Nd:Cr:YAG ceramics. Fairly broad bands below 240 nm are composed of band-to-band absorption and broad absorption due to the 4f-5d transitions of Nd^{3+} because the band-edge in pure YAG crystals is located around 180 nm. The sharp lines around 355 and 590 nm are due to the 4f-4f transitions of Nd^{3+} , while the broad band around 450 nm is due to the 3d-3d transition of Cr^{3+} .

Excitation below 240 nm in Nd:YAG ceramics produces several sharp lines of fluorescence in the visible (400-630 nm) and near-IR ranges, as shown in Fig. 2, being due to the transitions from ${}^2\text{F}_{5/2}$ and ${}^4\text{F}_{3/2}$ to other multiplets of Nd^{3+} , respectively. The near-UV and visible excitations produce only the near-IR fluorescence lines of Nd^{3+} . On the other hand, the excitation in Nd:Cr:YAG ceramics produces red fluorescence lines around 700 nm other than Nd^{3+} -lines. These lines are due to the ${}^2\text{E} \rightarrow {}^4\text{A}_2$ transition of Cr^{3+} .

Figure 3 shows the excitation spectra in Nd:YAG and Nd:Cr:YAG ceramics. The broad excitation bands of the visible Nd-fluorescence lines in Nd:YAG ceramics are due to the 4f-5d transition of Nd^{3+} . Similar excitation spectrum of the 400-nm Nd-fluorescence lines with five resolved bands were observed in Nd:Cr:YAG ceramics. The excitation spectrum of 707-nm Cr-fluorescence line is different from those of Nd-lines. The peaks of the Cr-bands are coincident with the bottoms of Nd-bands. This fact suggests that energy transfer occurs from Cr to Nd in Nd:Cr:YAG ceramics.

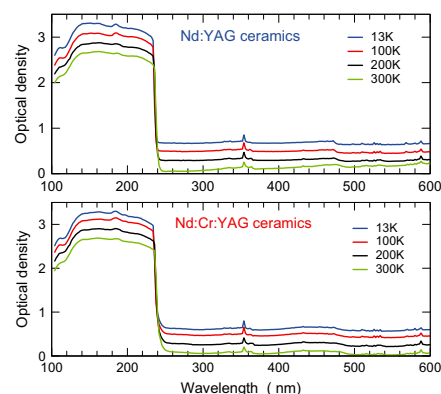


Fig. 1. Temperature dependence of absorption spectra for Nd:YAG and Nd:Cr:YAG ceramics.

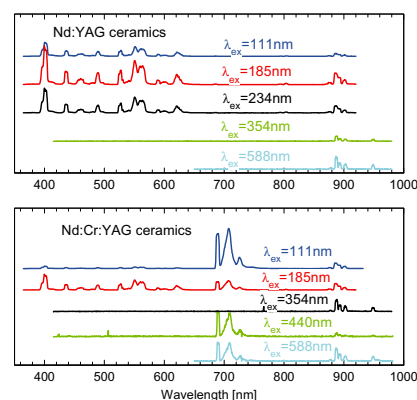


Fig. 2. Fluorescence spectra with various excitation wavelengths in Nd:YAG and Nd:Cr:YAG ceramics.

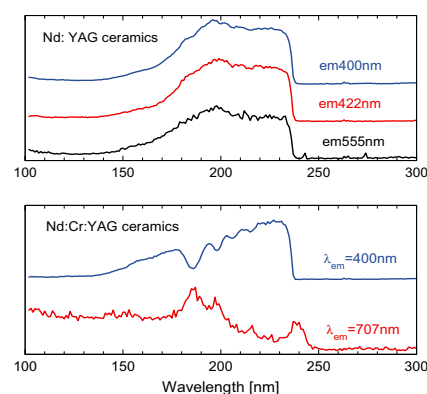


Fig. 3. Excitation spectra of Nd and Cr fluorescence in Nd:YAG and Nd:Cr:YAG ceramics.

Excitation and Emission Spectra for Ce^{3+} in SrY_2O_4

M. Yoshino¹, S. Watanabe² and Y. Ichikawa¹

¹ Department of Materials, Physics and Energy Engineering, Nagoya University, Nagoya 464-8603, Japan

² Department of Chemistry, Kwansai Gakuin University, Sanda 669-1337, Japan

The trivalent lanthanide ions (e.g. Nd^{3+} , Er^{3+} , Yb^{3+}) in Oxide crystals have drawn attentions due to their application for luminescent materials in NIR to UV regions such as solid-state lasers or phosphors. And, Ce^{3+} has also attracted attentions as luminescence centers. In this work, the $4f-5d$ excitation spectra and emission spectra for Ce^{3+} in SrY_2O_4 crystal have been measured. For the comparison, the excitation spectra and emission spectra for host oxide, SrY_2O_4 have been also measured. The Ce doped and pure SrY_2O_4 samples are produced by solid state reactions in 1373 K. The concentration of Ce^{3+} in the sample is 3 mol%. Figure 1 shows the emission spectrum for host oxide, SrY_2O_4 . The broad peaks from interband optical transition exist around 300-600 nm. Then the excitation spectrum monitored 423 nm is shown in

Fig. 2. The peak near 200 nm relates the absorption from the optical transition around the band edge in SrY_2O_4 . The emission spectra for Ce^{3+} in SrY_2O_4 are shown in Fig. 3. In case of the excitation wavelength is 200 nm so as to excite the host, the broad peak appears below the peak relates to the emission of SrY_2O_4 . The excitation spectrum monitored this emission (540 nm) is shown in Fig. 4. The broad peak appears below the peak relates to the absorption of SrY_2O_4 host. In case of the excitation wavelength is set in 320 nm so as to excite with the absorption band lies below the band edge absorption, only the broad peak around 600 nm appears as shown in Fig. 3. These emission and absorption peaks lie below the spectra relate to the host, are due to the Ce^{3+} $4f-5d$ transition.

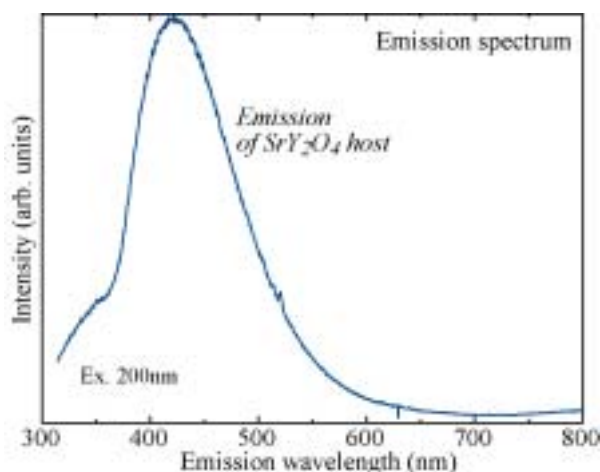


Fig. 1. Emission spectrum for SrY_2O_4 .

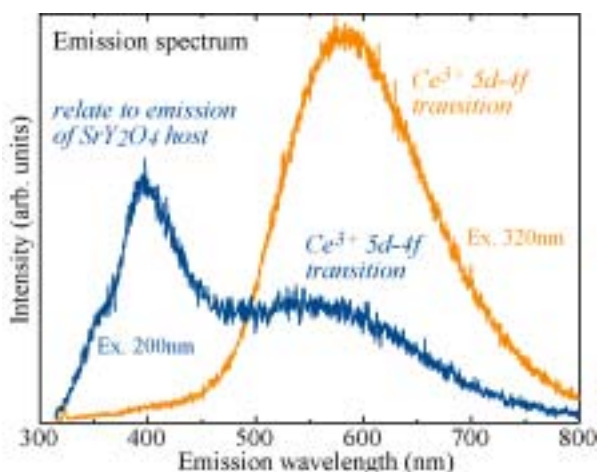


Fig. 3. Emission spectra for Ce^{3+} in SrY_2O_4 .

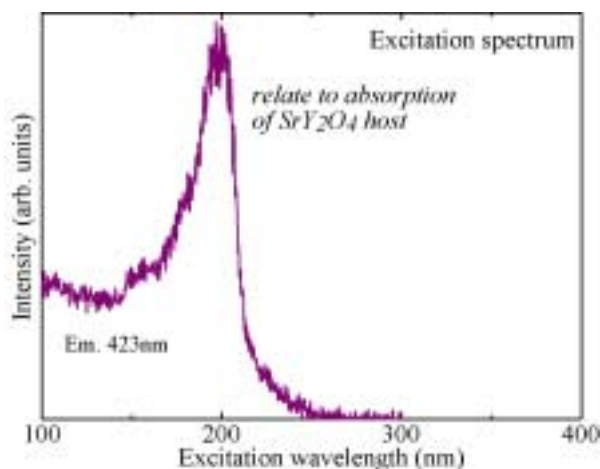


Fig. 2. Excitation spectrum for SrY_2O_4 .

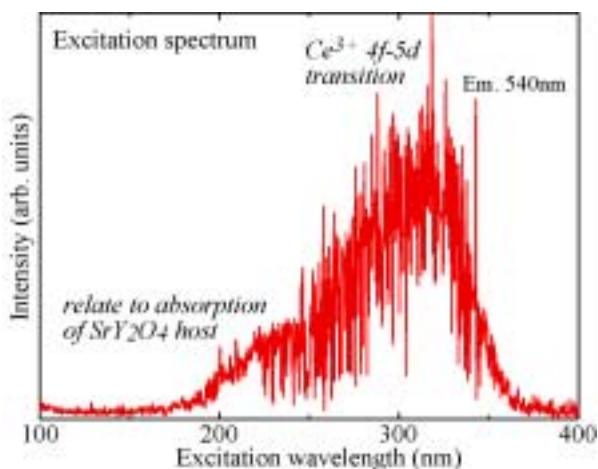


Fig. 4. Excitation spectrum for Ce^{3+} in SrY_2O_4 .

Charging Behavior of Li_2MnO_3 -Based Cathode Materials for Lithium-Ion Secondary Batteries from Metal L-Edge and Oxygen K-Edge Spectroscopy

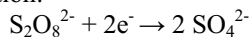
Y. Arachi, M. Nakamura, K. Hinoshita and Y. Higuchi

Faculty of Engineering, Kansai University, Osaka 564-8680, Japan

New potential cathode materials to replace LiCoO_2 in Li-ion batteries are under extensive investigation. $\text{LiNi}_{0.5}\text{Mn}_{0.5}\text{O}_2$ has been proposed as a promising cathode material with attractive properties. Cells using this material exhibit a reversible capacity of c.a. 150 mAh/g within the voltage range of 2.5 to 4.3 V. Furthermore, the material shows superior characteristics for larger capacities when compared to LiMn_2O_4 and for better thermal stability when compared to LiNiO_2 . This material is considered to be Li_2MnO_3 -based solid solutions containing Ni. In this study, we have investigated the Fe^{3+} containing compositions, $\text{Li}[\text{Li}_{1/3-x/2}\text{Fe}_{3x/2}\text{Mn}_{2/3-x}]\text{O}_2$ with layered NaCl-type structure. It is of great importance to understand the charging/discharging mechanism proceeding by Li-extraction/insertion. We have employed the variety of measurement techniques and specifically, examined the crystal structure and electronic structure using X-ray, neutron diffraction and XAFS measurements. In this study, the electronic structural changes were observed by XANES spectra of Fe, Mn L-edges and O K-edge respectively and the charging behavior was examined.

Experiment

$\text{Li}[\text{Li}_{1/3-x/2}\text{Fe}_{3x/2}\text{Mn}_{2/3-x}]\text{O}_2$ was prepared by co-precipitation method. $\text{LiOH}\cdot\text{H}_2\text{O}$ and precipitates of Fe, Mn hydroxides were mixed and then calcinated at 600°C for 12h. The obtained powders were pressed and sintered at $700\text{--}900^\circ\text{C}$ for 12h in air. De-lithiated samples were electrochemically and chemically prepared. The former was used by coin-type cells with $\text{Li}/1\text{M LiPF}_6$ in $\text{PC}:\text{DMC}(1:1)$ /samples and the latter was by the chemical oxidants, ammonium persulfate as the following reaction:



$\text{Li}_{1.2}\text{Fe}_{0.4}\text{Mn}_{0.4}\text{O}_2 \rightarrow \text{Li}_{1.2-x}\text{Fe}_{0.4}\text{Mn}_{0.4}\text{O}_2 + x\text{Li}^+ + x\text{e}^-$
X-ray absorption measurements at the Fe, Mn L-edges and O K-edge by total electron yield were performed on BL4B and BL8B1.

Results

Figures 1 and 2 show the selected XANES spectra of Fe L-edge for chemically and electrochemically oxidized $\text{Li}_{1.2-x}\text{Fe}_{0.4}\text{Mn}_{0.4}\text{O}_2$ respectively. The notation from CdeLi1 to CdeLi3 corresponds to the reaction time of 0.1 to 1.0 h at various steps. A remarkable difference is observed between these two results. As the samples are oxidized, a shift towards higher energy is clearly observed for chemically oxidized, but not for electrochemically. thresholds, which are completely absent from the ion yield spectrum. A similar enhancement of the neutral

particle yield is observed around the N 1s ionization. Electrochemical reaction occurs from the surface of the electrode. In contrast, chemical oxidation reaction proceeds throughout the sample. This result will strongly support the electrochemical properties for this material which shows a large irreversible capacity in the initial cycle. It indicates that an inhomogeneous reaction may occur on the surface of cathode materials.

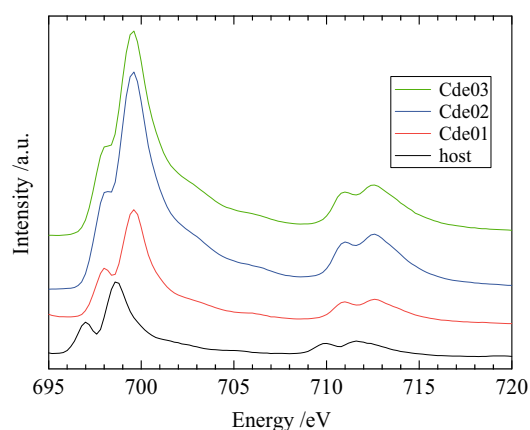


Fig.1. Fe L-edge XANES spectra of chemically oxidized $\text{Li}_{1.2-x}\text{Fe}_{0.4}\text{Mn}_{0.4}\text{O}_2$.

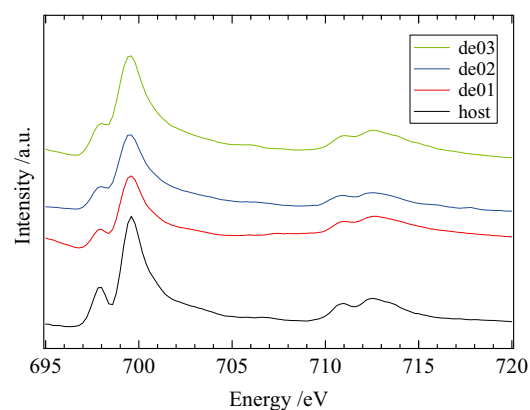


Fig. 2. Fe L-edge XANES spectra of electrochemically oxidized $\text{Li}_{1.2-x}\text{Fe}_{0.4}\text{Mn}_{0.4}\text{O}_2$.

XAFS Study on the Surface Structures of the Positive Electrodes for High Power-Type Lithium-Ion Battery Cells

M. Shikano and H. Nitani

Research Institute for Ubiquitous Energy Devices, AIST, Ikeda, Osaka 563-8577, Japan

Introduction

Lithium-ion battery is one of the key component of fuel cell vehicles (FCVs), hybrid electric vehicles (HEVs), plug-in HEVs (PHEVs), and battery electric vehicles. In particular, for FCV, HEV and PHEV application, high specific power ($> 1\text{--}2$ kW/kg), long calendar life (> 10 years) and safety are very important requirements. In our previous work, degradation mechanism of lithium-ion batteries for HEV usage has been studied by various analyzing techniques and we concluded that the major factor of power fade was degradation of positive electrode structure near the surface [1-4]. However, the mechanism of degradation of the positive electrodes is still poorly understood. Detailed analysis on the structural changes of electrode material is essential in order to determine the origin of the degradation of battery performance.

In this study, LiNiO_2 -based positive electrodes ($\text{Li}(\text{NiCoAl})\text{O}_2$) in the initial cells were examined by X-ray absorption fine structure (XAFS) measurements to obtain information on the surface of the positive electrode.

Experimental

Cylindrical lithium-ion cells were used in this study. After adjusting the state of charge (SOC) of cell, the cells were disassembled under dry argon atmosphere in order to obtain materials. The obtained positive electrodes were washed by DMC and then dried under vacuum. Then the washed electrodes were cut into small pieces and fixed onto the aluminum plate by carbon tape.

XAFS spectra of these positive electrodes were measured at UVSOR BL4B for Co and Ni LIII-edge. All measurements were performed with Total Electron Yield (TEY) technique by measuring the sample current in vacuumed chamber at room temperature. Obtained XAFS spectra data were processed with Athena 0.8.057 software.

Results

Figure 1 shows typical Co and Ni LIII-edge X-ray absorption near-edge structure (XANES) spectra obtained of the positive electrodes. We could obtain good spectrum with very high energy-resolution. Especially, the double peak structure was clearly observed in Ni LIII-edge spectrum. This feature means that Ni atoms existed with mixed atomic valences in the electrode sample. Furthermore, we found that the shape of this double peak drastically changes depends on the SOC of battery cell before disassembling (figure is not shown). The more detailed structural analysis and *ab initio* calculation are in progress in

order to understand these changes in the XANES spectra.

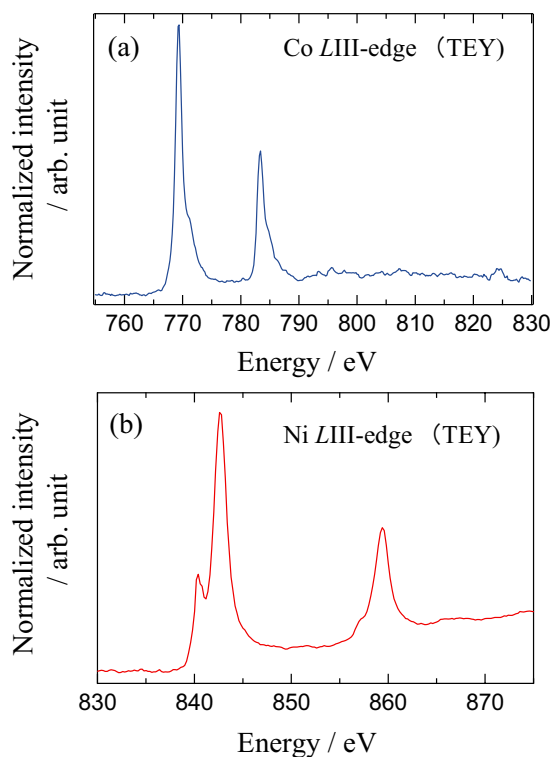


Fig. 1. (a) Co LIII-edge and (b) Ni LIII-edge XANES spectra of positive electrode (SOC90%).

- [1] H. Kobayashi, M. Shikano, S. Koike, H. Sakaebe and K. Tatsumi, *J. Power Sources* **174** (2007) 380.
- [2] M. Shikano, H. Kobayashi, S. Koike, H. Sakaebe, E. Ikenaga, K. Kobayashi and K. Tatsumi, *J. Power Sources* **174** (2007) 795.
- [3] M. Rahman and Y. Saito, *J. Power Sources* **174** (2007) 889.
- [4] Y. Saito and M. Rahman, *J. Power Sources* **174** (2007) 877.

Photoinduced Change in the Total Photoyield of Amorphous Materials by Irradiation of Bandgap Light

K. Hayashi

Department of Electrical and Electronic Engineering, Gifu University, Gifu 501-1193, Japan

Introduction

The photoinduced change in photoconductivity during and after irradiation of bandgap light has been observed in many amorphous materials. [1, 2] This phenomenon is usually called the photodegradation and is explained in terms of photoinduced metastable defects. The creation of defects is a serious problem in the device application of these materials. The photodarkening is also a well-known phenomenon in amorphous chalcogenide materials. The photodarkening is a parallel shift to the optical absorption edge to lower energy side after irradiation of bandgap light. This darkened state is removed by annealing near the glass-transition temperature. The x-ray diffraction and the volume change of the films before and after irradiation of bandgap light suggest that photodarkening is due to a change of the local structure of the amorphous network. [3-5] Although a large number of studies have been done on the photoinduced phenomena, details of their underlying mechanisms are still not clear. Understanding the physical mechanisms of their underlying metastability is one of the fundamental problems associated with these materials.

The measurement of the total photoyield at the vacuum ultra-violet region is a powerful tool for the study of the energy structure. The photoyield will reflect optical absorption and the photoconductivity of the material. In this report, we investigate photoinduced change in the total photoyield of amorphous chalcogenide films.

Experimental

Thin films of amorphous chalcogenide materials ($a\text{-As}_2\text{S}_3$ and $a\text{-As}_2\text{Se}_3$) were prepared onto quartz substrates which fabricated Au electrodes by conventional evaporation technique. A typical thickness of an amorphous film was around 300 nm. The samples were annealed at the almost glass-transition temperature for two hours in a vacuum. A xenon arc lamp with IR-cut-off filter was used as a bandgap light source. The measurements of the total photoyield were performed at room temperature at the BL5B beam line of the UVSOR facility. The VUV light was fixed to the wavelength that was able to excite 3d core level of As atom of each material. To eliminate the higher order light from the monochromator, an aluminum thin film and a pinhole of 1.5 mm in a diameter were inserted between the monochromator and sample. We also monitored the intensity of the VUV light by measuring the total photoyield of two gold meshes.

Results and Discussion

Figure 1 shows the photoinduced change in the total photoyield of an $a\text{-As}_2\text{S}_3$ film by irradiation of bandgap light. This figure is obtained by normalizing the photoyield by the incident photon flux measured with Au mesh (Au-U) of the upstream. As shown in the figure, after irradiation of bandgap light the photoyield is gradually increased and it seems to be finally saturated. This change is similar to the previous report [6] in the total photoyield by irradiation of VUV light from the undulator light source. The relation among this photoyield change, the photodegradation, and the photodarkening will be more clarified in the next step.

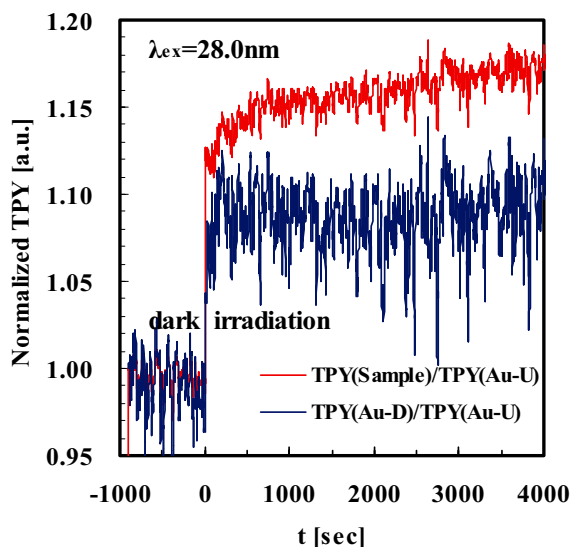


Fig. 1. The photoinduced change in the total photoyield of an $a\text{-As}_2\text{S}_3$ film by irradiation of bandgap light.

Acknowledgements

This work was partly supported by Saijiro Endo Memorial Foundation for Science & Technology.

- [1] D. L. Staebler and C.R. Wronski, *Appl. Phys. Lett.* **31** (1977) 292.
- [2] K. Shimakawa, S. Inami and S.R. Elliott, *Phys. Rev. B* **42** (1990) 11857.
- [3] K. Tanaka, *Rev. Solid State Sci.* **4** (1990) 641.
- [4] J. P. De Neuvile, S.C. Moss and S. R. Ovsinsky, *J. Non-Cryst. Solids* **13** (1973/1974) 191.
- [5] A. J. Lowe, S. R. Elliot and G. N. Greaves, *Philos. Mag.* **54** (1986) 483.
- [6] K. Hayashi, *UVSOR Activity Report* **25** (1998) 118.

Characterization of Novel Oxide Multilayer Reflectors at "Water-Window" Wavelengths Fabricated by Atomic Layer Epitaxy

H. Kumagai¹, Y. Masuda¹, Y. Tanaka¹, T. Shinagawa² and A. Kobayashi¹

¹Graduate School of Engineering, Osaka City University, Sumiyoshi-ku, Osaka 558-8585, Japan

²Inorganic Materials Lab., Osaka Municipal Technical Research Institute, Joto-ku, Osaka 536-8553, Japan

Since Barbee et al. successfully demonstrated near-normal-incidence ($\theta=15.5^\circ$) soft-x-ray reflectors with high reflectances of 67% at 17.0 nm using 20-bilayer Mo/Si multilayers deposited by magnetron sputtering [1], there have been various studies on the fabrication of soft-x-ray multilayer reflectors using electron beam evaporation and ion beam, rf and dc magnetron sputtering deposition. In particular, development of high-performance normal-incidence multilayer optics for the water-window wavelength region between the oxygen and carbon K absorption edges at 2.33 and 4.36 nm, respectively, where water is relatively transmissive and organic materials are absorptive, has been a technical challenge of great interest. The extremely small periods (1.2-2.2 nm) of soft-x-ray reflectors require very rigorous specifications to be met with respect to interface roughness and interlayer mixing, because interface roughness on an atomic scale has a substantial effect on soft-x-ray reflectance. Therefore, the highest reflectance achieved at water-window wavelengths ($\theta=3.18^\circ$) and near normal incidence ($\theta=9^\circ$) has been 3.3% [2], in spite of the various efforts which have been made in this field. The reason that the reflectances achieved at these wavelengths are so low is that the Fresnel coefficients of materials are so small at these wavelengths that a large number of bilayers must be used, which means that the problems of interface roughness and imperfect interfaces due to interlayer mixing become serious.

The authors have proposed the use of a novel metal oxide multilayer for soft-x-ray reflectors at water-window wavelengths [3], because an oxide multilayer can prevent the formation of an alloy at the interface, and the absorption of oxygen in oxides is negligible at the water-window wavelengths; moreover, the metal oxide multilayer can be fabricated by the atomic layer deposition or atomic layer epitaxy technique. These techniques can be used to control surfaces on an atomic scale by sequentially dosing the surface with appropriate chemical precursors and then promoting surface chemical reactions which are inherently self-limiting. We have found that the self-limiting adsorption mechanism works in the fabrication of oxide thin films such as aluminum oxide and titanium oxide. And we reported that we have experimentally demonstrated high reflectance of over 30% at a wavelength of 2.734 nm and an incident angle of 71.8° from the normal

incidence using novel metal oxide multilayers of titanium oxide and aluminum oxide fabricated by the atomic layer deposition method of controlled growth with sequential surface chemical reactions.

In this study, the authors also demonstrated that novel oxide superlattice structures of crystalline ZnO/TiO₂ on sapphire substrates were fabricated for high-reflection multilayer mirrors at 2.734 nm. Theoretical calculations also indicated that these structures could give high reflectance over 50% at the wavelength. In the experimental study, both rutile TiO₂ (200) and wurtzite ZnO (0001) thin films were grown epitaxially on the same sapphire (0001) substrates by atomic layer epitaxy (ALE) at 450°C. We demonstrated for the first time that the novel oxide superlattice structure of 10-bilayer ZnO/TiO₂ on a sapphire substrate gave high reflectance of 33% at a wavelength of 2.734 nm, as shown in Fig. 1.

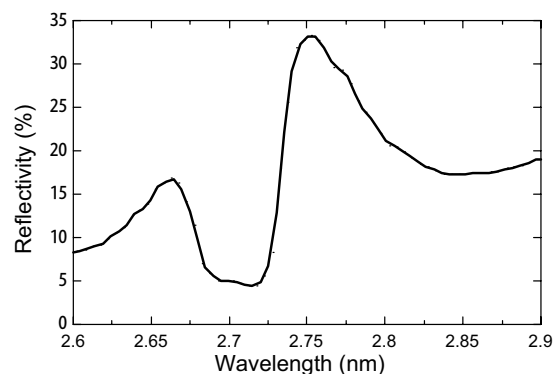


Fig. 1. Experimental reflectances of the ALE-grown 10-bilayer ZnO/TiO₂ structure on a sapphire (0001) substrate. $\theta=86^\circ$.

- [1] T. W. Barbee, Jr. *et al.*, *Appl. Opt.* **24** (1985) 883.
 [2] J. F. Seely *et al.*, *Appl. Opt.* **32** (1993) 3541.
 [3] H. Kumagai *et al.*, *Appl. Phys. Lett.* **70** (1997) 2338.

Measurement of Absolute Efficiency for Micro Channel Plates by Using Pure-Calibrated EUV Beam

G. Ogawa, K. Yoshioka, G. Murakami and I. Yoshikawa

*Department of Earth and Planetary Science, Graduate School of Science,
The University of Tokyo, Tokyo 113-0033, Japan*

Introduction

We study to optically observe the Earth's plasmasphere, which is filled with cold plasmas (mainly H⁺, He⁺, O⁺ and electrons). The He⁺ and O⁺ ions have resonance scattering emission lines in the extreme ultraviolet region, at 30.4nm (HeII) and 83.4nm (OII) respectively. The intensity of each emission is proportional to column density of each scattered particle under the assumption of the optically thin condition.

EUVI (Extremity Ultra-Violet Imager) for the ISS-IMAP mission (Ionosphere, Mesosphere, upper Atmosphere and Plasmasphere mapping onboard the International Space Station) is under development. The instrument consists of two detectors, EUVI-HeII and EUVI-OII. The former observes resonantly-scattered light from He⁺ and the latter observes resonantly-scattered light from O⁺ in the plasmasphere. Both of them have band-pass filters and micro channel plates (MCPs), and look for the direction of the earth's limb. So, they can take images of the distribution of those ions in the plasmasphere over the limb.

The ISS-IMAP mission can make long-term (more than half year) and steady observations of the vertical and horizontal structure of the plasmasphere by using EUV light that cannot be observed on the ground. Furthermore, it can take images with higher special resolution comparing to the conventional spacecraft missions because the orbit of the ISS is closer to the plasmasphere than that of the other missions. So the ISS-IMAP mission will make up the interactions of the solar wind magnetic field variations and plasma transportation such as the supply from the ionosphere, piling up and the ejection of the plasmas in the plasmasphere.

It is very important to get the absolute efficiency of the instrument in order to grasp the plasma density properly. In this experiment, we measure the quantum efficiency of the MCPs, which we use as the standard detector, at 30.4nm line.

Measurement and Result

We install an Al/C (1201Å/54Å) filter on the entrance of the SOR beam to eliminate the multi-order lines from 30.4nm line with PGM35. At first, we investigate the purity of the 30.4nm line through the Al/C filter. We judge the purity from the consistency between the wavelength characteristics of an Al/C filter for the particular lines at the EUV facilities of Institute of Space and Astronautical

Science (ISAS) and those for the continuous lines at UVSOR. The former is measured for the emission lines of the helium gas with the discharge light source. Figure 1 shows the transmittances of the filter measured at ISAS and UVSOR. It is clear that both profiles of the filter are consistent in the wavelength region of 20-50nm. We interpret from the result that the pure 30.4nm can be introduced through the Al/C filter by using PGM35.

With the available pure 30.4nm line, then we measure the quantum efficiency of the MCPs. The quantum efficiency is calculated by the rate of the MCPs count to the electron yield of the photo diode which is absolutely calibrated. The result of the measurement shows that the quantum efficiency of the MCPs is 11.3% at 30.4nm line.

For the next step, in addition to the 30.4nm line, we plan to measure the quantum efficiency at the 83.4nm line, which is another observational object of EUVI. Then the purity of 83.4nm line is essential, and must be investigated for the next machine time.

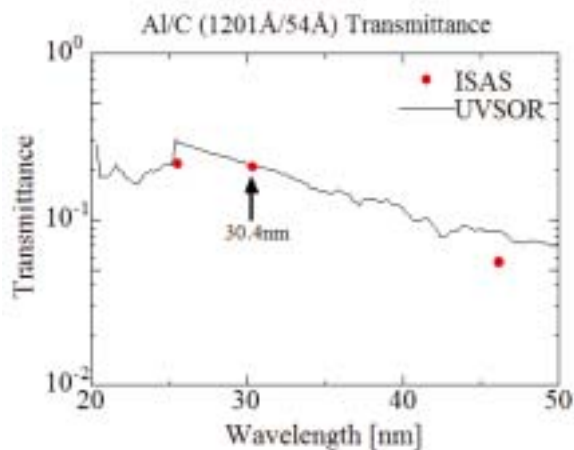


Fig. 1. The transmittance of an Al/C (1201Å/54Å) filter. The red dots show the results of the measurements at the EUV facility of ISAS and the solid line shows that at UVSOR.

[1] G. Murakami, K. Yoshioka, K. Hikosaka, A. Yamazaki and I. Yoshikawa, UVSOR activity report **34** (2007) 47.

[2] K. Yoshioka, G. Murakami, T. Toyota, G. Ogawa, A. Yamazaki and I. Yoshikawa, UVSOR activity report **35** (2008) 55.

Far-Infrared Reflective Study of Alkali Niobate Ceramics

H. Matsudo, Y. Inagaki, T. Sumi, I. Kagomiya and K. Kakimoto

*Graduate School of Engineering, Nagoya Institute of Technology, Showa-ku, Nagoya
466-8555, Japan*

Introduction

$(\text{Na}_{0.5}\text{K}_{0.5})\text{NbO}_3\text{-LiNbO}_3$ (LNKN) is one of promising candidates of lead-free piezoelectric material because it shows the excellent piezoelectric property of $d_{33}=235$ pC/N when the Li content is 6.0 mol% [1]. The phase transition of LNKN varied with the content of Li, and it is considered that the phase transition between tetragonal and orthorhombic exist at the Li content of 5-7 mol% range at room temperature. LNKN undergoes the temperature-dependent successive phase transition. In our previous study, phase transition of LNKN was studied by using Raman scattering to clarify the origin of good piezoelectric property [2,3]. In this study, IR reflectivity of LNKN ceramics was measured in order to understand the effect of Li incorporation against the lattice vibration of LNKN.

Experimental procedure

The ceramic samples were sintered by the ordinal solid state reaction method. In this study, $\text{Li}_{0.06}(\text{Na}_{0.5}\text{K}_{0.5})_{0.94}\text{NbO}_3$ (L6) and $\text{Na}_{0.5}\text{K}_{0.5}\text{NbO}_3$ (NKN) were used for IR reflective study. The ceramics were polished to become specular surfaces.

Reflectivity far-infrared spectra of L6 and NKN ceramic samples were obtained at 78 and 300 K at the BL6B beam line of UVSOR. The spectra were corrected by using Michelson interferometer (Bruker, IFS66v) and synchrotron radiation source.

Result and Discussion

Figure 1 shows far-infrared reflectivity spectra of NKN at 78 and 300 K. Broad absorption was observed from 150 to 200 cm^{-1} at 300 K. This absorption was attributed by TO phonon of the vibration of Na and K ions against the NbO_6 unit. In addition, another absorption around 120 cm^{-1} was observed at 78 K. NKN shows the phase transition from rhombohedral to orthorhombic crystal structure at 125 K on heating process so that the phase transition of NKN includes the softening of translational modes of Na and K ions.

Figure 2 shows far-infrared reflectivity spectra of L6 at 78 and 300 K. The absorption of translational modes of Na and K ions were not clear and the softening of the translational modes was not observed between the spectrum at 78 K and that at 300 K in spite that the phase transition from rhombohedral to orthorhombic crystal structure exists at 270 K. In our previous study, Raman spectroscopy confirmed that NbO_6 unit received an internal strain by increasing Li content [3]. It is believed that the distortion of NbO_6 ,

which was induced by the small ion of Li, causes the suppression of the translational vibration of Na and K ions in unit-cell crystal structure.

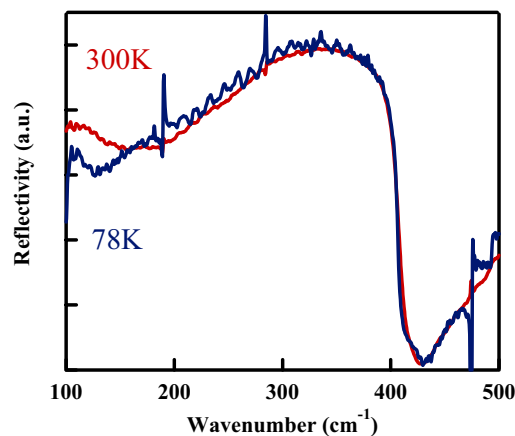


Fig. 1. Far-infrared reflectivity spectra of NKN ceramics at 78 and 300 K.

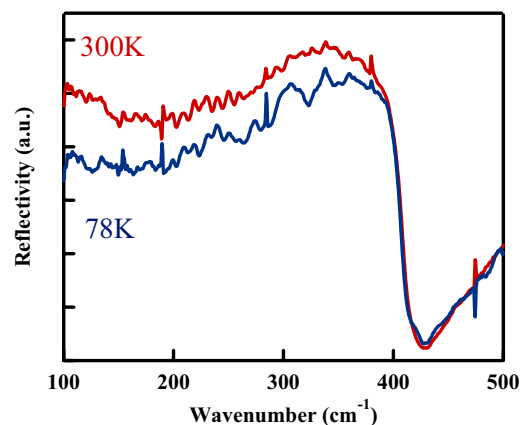


Fig. 2. Far-infrared reflectivity spectra of L6 ceramics at 78 and 300 K.

Acknowledgement

This research was supported by the Industrial Technology Research Grant Program in 2007 from the New Energy and Industrial Technology Development Organization (NEDO) of Japan.

- [1] Y. Guo, K. Kakimoto and H. Ohsato, *Appl. Phys. Lett.* **85** (2002) 4121.
- [2] K. Kakimoto, K. Akao, Y. Guo and H. Ohsato, *Jpn. J. Appl. Phys.* **44** (2005) 7064.
- [3] T. Hotta, K. Kakimoto and H. Ohsato, *Key Eng. Mater.* **368-372** (2008) 1893.

Characterization of Highly Efficient Dye Sensitized Solar Cells Using Synchrotron Radiation

K. Nakajima^{1,2}, H. Yagi², C. Huang², H. Katayanagi² and K. Mitsuke²

¹Science Research Center, Hosei University, Tokyo 102-8160, Japan

²Department of Photo-Molecular Science, Institute for Molecular Science, Okazaki 444-8585, Japan

About two decades ago Grätzel et al. [1] first invented the dye sensitized solar cell (DSSC) with energy conversion efficiency of more than 10 %. Thereafter many relevant works have been reported, but significant improvement in the efficiency has not been achieved yet. In the present study we assembled DSSCs using a Ru dye and made them irradiated with monochromatized synchrotron radiation to observe electron injection process occurring at the interface between the dyes and semiconductor nanoparticles. The measurements of photoabsorption cross sections and output short-circuit currents by irradiation of synchrotron light allowed us to determine an incident photon-to-current efficiency (IPCE) of the DSSC and an absorbed photon-to-current efficiency (APCE) of the dye. The IPCE is calculated from the number of electrons $J_{SC}S/e$ fed into an external circuit divided by that of incident photons on the cell, $\Phi_p = I_p S = PS/h\nu$. The APCE is derived from $J_{SC}S/e$ divided by the number of photons absorbed by the sensitizer dye $\Delta\Phi_p$. Here, J_{SC} is the density of the output short-circuit current, S is the area of the DSSC, e is the elementary charge, I_p is the intensity of the incident photon, and P is the power density of the synchrotron radiation.

The DSSC was prepared as follows. Titanium dioxide TiO_2 paste (nanoparticles, 18 nm in diameter) was applied on an FTO glass by screen printing, and sintered at 450°C for 30 min. After soaking the glass in a Ru dye solution (N3 or N719), iodide electrolyte (PN-50 or AN-50) was dropped on the TiO_2 electrode which was combined with a counter electrode glass covered with Pt. Our DSSC exhibits a maximum energy conversion efficiency of about 7 %.

Figure 1 (a) shows an IPCE curve obtained from J_{SC} and Φ_p . Since the curve is in accordance with the curve (b) that was obtained using an instrument dedicated for the IPCE measurements (Peccell: PEC-S20DC), it was confirmed that synchrotron radiation can be used for the measurement of IPCE even though its flux is 2 – 3 orders of magnitude lower than that of the Xe lamp fitted in the above instrument. An IPCE value was improved to 0.7 when the layer of TiO_2 film is thicker than 16 μm . Figure 2 shows the two APCE curves calculated in different ways of estimation of $\Delta\Phi_p$, according as whether the scattered light in the TiO_2 film is partly absorbed by dye (b) or not (a). It is clear that such a reabsorption

may favorably take place in a shorter wavelength and contributes to electron injection from the dye. The quantum yield of the electron injection is evaluated to be unity at shorter wavelengths, whereas it gradually decreases in longer wavelength.

The energy conversion efficiency of the DSSC will be improved when an appropriate conductive glass is selected and the best condition for sintering of a TiO_2 film is established. We are planning to observe fluorescence from the dye molecules adsorbed on several semiconductor films to study the rate of electron injection to TiO_2 film from the dye.

This research was partly supported by a grant from Hosei University.

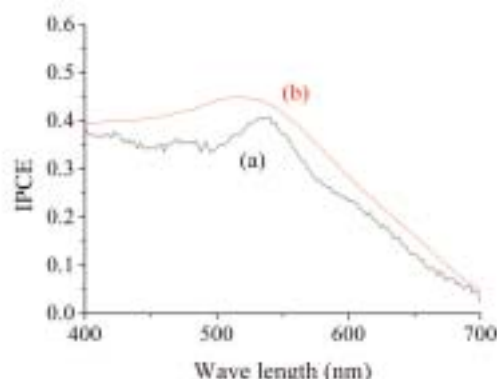


Fig. 1. IPCE curves obtained by (a) synchrotron radiation and (b) the PEC-S20DC spectrometer.

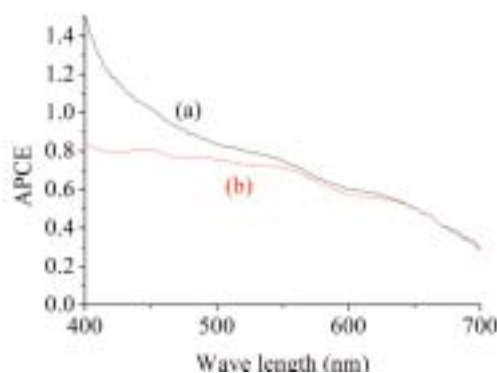


Fig. 2. Variation of APCE curves in different estimation of photons absorbed by dye.

[1] B. O'Regan, M. Grätzel, Nature **353** (1991) 737.

Reflection Measurement on Si/W/Co and Si/W/C Multilayers for Use in 50-110 nm Region

T. Ejima¹, F. Suzuki², K. Fukui², M. Yanagihara¹, Z. Wang³, J. Zhu³, L. Bai³, Z. Zhang³, Q. Huang³, J. Xu³, X. Wang³ and M. Watanabe^{4,5,6}

¹IMRAM, Tohoku University, Sendai 980-8577, Japan

²Faculty of Engineering, University of Fukui, Fukui 910-8507, Japan

³Institute of Precision Optical Engineering, Tongji University, Shanghai 200092, China

⁴Shanghai Dianji University, Shanghai 200240, China

⁵Institute for Composite Materials, Shanghai Jiaotong University, Shanghai 200240, China

⁶Venture Business Laboratory, Saga University, Saga 840-8402, Japan

High normal-incidence reflectivity mirrors with a flat top in 50–110 nm region are required not only for usual spectroscopy, but also some diagnosis of plasma. In this region, monolayers of Au, Pt and W are used as coating materials. Their reflectivity is about 30% and decreases around 50 nm down to 20% or less. The reflectivity of monolayer of SiC is higher than 40%, but the high reflectivity region is limited above 60 nm. Therefore, special multilayers are required to obtain such high reflectivity in this region. Composite multilayers consisting of a top single layer and piled periodic double layers have been developed to extend the region of reflectivity of more than 15% down to 30 nm [1], but their reflectivity around 50 nm is 20%. In this study, availability of non-periodic multilayers [2] has been investigated.

The multilayers were $[\text{Si}/\text{W}/\text{Co}]_2$ and $[\text{Si}/\text{W}/\text{C}]_2$. Here the subscript “2” means 2 trilayers of different layer thicknesses. In both multilayers, the top layers were Si layers and the substrates were Si wafer. The multilayers were designed to have high reflectivity of 40–50% in this region at incident angle of 5°, which has not been obtained so far. In $[\text{Si}/\text{W}/\text{Co}]_2$, the designed value of layer thickness was respectively 8.96, 11.57, 6.07, 19.01, 12.47 and 11.68 nm from the top Si layer, and in $[\text{Si}/\text{W}/\text{C}]_2$, 9.41, 3, 15.83, 23.48, 3, 14.42 nm. They were fabricated by magnetron sputtering at Tongji University. Near normal incidence reflectivity was measured at BL7B, which is equipped with a 3 m McPherson type monochromator. The p-reflectivity was measured at incident angles of 20° and 30°.

Figures 1 and 2 show the experimental and calculated reflectivity of $[\text{Si}/\text{W}/\text{Co}]_2$ and $[\text{Si}/\text{W}/\text{C}]_2$ multilayers for incident angle of 20°. The reflectivity was measured with good reproducibility. The calculated reflectivity is smaller at incident angle of 20° than 5°. It is due to the measurement of p-reflectivity. The experimental results at incident angle of 20° show the reflectivity of 50–60% of the calculated values. For investigation of this reason, the X-ray diffraction measurements on the multilayers were made to determine the actual layer thicknesses. It was found that the actual thicknesses did not deviate much more from the designed value except the top layers. On the top layers, about 2 nm SiO_2

layers were found. Taking into account this fact, the recalculation was performed and the discrepancy between experimental value and calculated value was well explained. It is an important subject of the next step how to reduce the amount of SiO_2 .

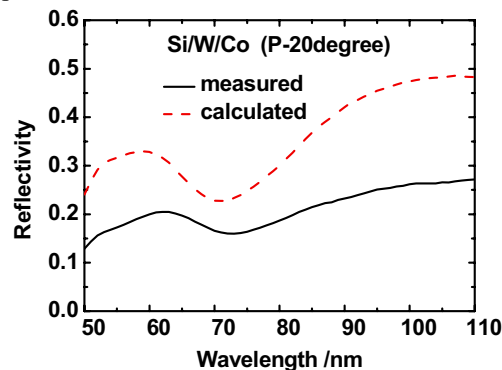


Fig. 1. Calculated and measured reflectivity of Si/W/Co multilayer at incident angle of 20°.

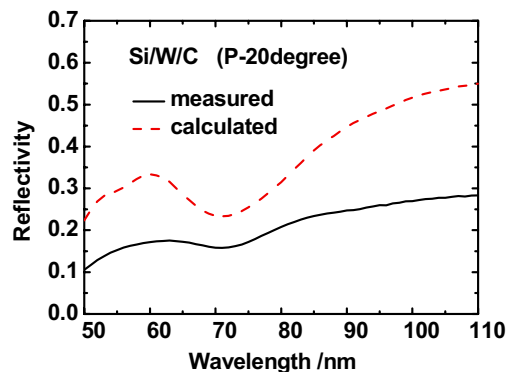


Fig. 2. Calculated and measured reflectivity of Si/W/C multilayer at incident angle of 20°.

[1] Y. Kondo *et al*, Nucl. Instr. Meth. A **467-468** (2001) 333.

[2] Z. Wang *et al.*, J. Appl. Phys. **99** (2006) 056108.